Experimental testing and analytical modelling of glulam moment connections with self-drilling dowels

Wenchen Dong[1], Minghao Li[2], Minjuan He[3], and Zheng Li[4]

[1]Department of Civil and Natural Resources Engineering, University of Canterbury, New Zealand. Email: wenchen.dong@pg.canterbury.ac.nz

[2]Department of Civil and Natural Resources Engineering, University of Canterbury, New Zealand.

[3]Department of Structural Engineering, Tongji University, China.

[4]Department of Structural Engineering, Tongji University, China.

ABSTRACT

An experimental and analytical study on rotational behaviour of glulam beam-column moment connections with self-drilling dowels (SDD) was conducted. Connection properties including strength, stiffness, ductility and energy dissipation were experimentally evaluated by testing seven full-scale connection specimens with and without self-tapping screw (STS) reinforcement along timber perpendicular to grain. All the connections showed high initial stiffness and high moment capacity when compared with the test results of bolted connections reported in literature. The unreinforced connections had relatively low ductility due to timber splitting despite the increased fastener edge distance. The STS reinforcement effectively reduced timber splitting tendency and encouraged the yielding of more SDD, leading to slightly increased moment capacity, but significantly improved ductility. A modified analytical model (MAM) was then proposed to predict strength and rotation of the SDD moment connections based on force and moment equilibrium of the glulam members. Improved prediction accuracy was achieved for the SDD moment connections when compared with the past analytical methods.

Keywords: Glulam, beam-column connections, moment capacity, self-drilling dowels, experimental testing, analytical model

INTRODUCTION

With increased availability of engineered wood products, such as, glue-laminated timber (glulam), laminated veneer lumber (LVL) and cross laminated timber (CLT), heavy timber structures are becoming more popular around the world (Sun et al. 2020). One of the widely used forms in heavy timber structures is the post-and-beam system due to its architectural flexibility and aesthetic appearance. Dowel-type connections consisting of bolts or dowels and inserted steel plates are commonly used in heavy timber frames. Design standards such as Eurocode 5 (2004) provide detailed design formulas for dowel-type connections with one inserted steel plate based on the Johansen's theory (Johansen 1949). Brittle failures are avoided by satisfying minimum spacing requirements for most cases. However, current standards do not have specifications explicitly for dowel-type connections with two or more inserted steel plates that can substantially increase the number of shear planes and the connection capacity. To apply these connections in practical design, the design formulas in Eurocode 5 (2004) were extended to consider scenarios with multiple inserted steel plates and verified by experimental tests (Sawata et al. 2006; Fan et al. 2011). Experimental testing of dowel-type moment connections (mostly bolted connections) has been carried out by Awaludin et al. (2007), Lam et al. (2008), Wang et al. (2015), Karagiannis et al. (2017), He et al. (2017), Zhang (2018), Wang et al. (2019) and Shu et al. (2019). These studies showed that the connections using bolts or conventional smooth dowels had initial slips and low initial stiffness mainly caused by over-sized predrilled holes for fastener installation tolerance. In addition, brittle failures such as timber splitting were observed, causing low connection ductility although the minimum spacing requirements were met. In this regard, it becomes very challenging to design ductile heavy timber moment frames in seismic regions. An alternative is to add shear walls or braces into timber frames, which however may restrict the flexibility of architectural plans. Therefore, there is a demand for improving the moment capacity and ductility of moment connections in timber frames. An innovative solution is the post-tensioning timber (Pres-Lam) beam-column connections where unbonded steel tendons pass through internal ducts in timber beams and columns to connect them by post-tensioning instead of dowel-type fasteners. Dissipation devices are usually attached to pro-

vide extra damping and moment capacity (Granello et al. 2020). Experimental tests of Pres-Lam beam-column connections and frames have been conducted for LVL (Palermo et al. 2005, Iqbal et al. 2016, Newcombe et al. 2010, Pino et al. 2010) and glulam (Smith et al. 2014, Wanninger and Frangi 2016, Li et al. 2018, Di Cesare et al. 2017). Test results showed good self-centring capacity without significant damage. However, different beam-column connection details can result in a huge variation of post-tensioning loss (Granello et al. 2018), which might affect the self-centering capability and cause the early activation of the dissipation devices (Granello et al. 2020). More research is suggested for the optimization of connection detailing and long-term performance of the system (Granello et al. 2020). Another solution is the ductile moment connection with glue-in rods. Some experimental tests have been carried out on them with different detailing (Buchanan and Fairweather 1993, Madhoushi and Ansell 2003, Vašek 2008, Fragiacomo and Batchelar 2012, Gilbert and Erochko 2019) and test results showed high stiffness and ductile performance could be achieved with good connection detailing. However, an agreement regarding design criteria for these connections has not been reached (Tlustochowicz et al. 2011) and it is not convenient for the in-situ gluing process (Yang et al. 2016). As one of the most widely-used connections, dowel-type connections that have been included in most standards are still preferred by engineers. Therefore, there is a demand for improving the moment capacity of dowel-type connections.

To overcome the initial slip issue of dowel-type connections caused by oversized holes, two methods were proposed in literature. One is to fill the gaps between the fasteners and the oversized holes by injecting resin (Rodd 1996). However, it requires strict quality control and drilling additional injection holes as well as vent holes can be time-consuming (Rodd and Leijten 2003). The other method is to use hollow steel tubes as fasteners and expand the diameter of the fasteners once installed to achieve a tight fit (Leijten 1998). The experimental tests showed that this type of connections could achieve high stiffness (van Bakel et al. 2017). Nevertheless, expanding the hollow steel tubes usually introduces high pre-stresses and the installation requires special gears including hydraulic jacks and specially shaped dies (Leijten and Brandon 2013). He et al. (2016) investigated one type of pre-stressed tube-bolted connection made of tight-fit two-layer tubes and high-strength

steel bolts. The connections were easy to assemble and the initial stiffness relied on the friction between the bolts and the tubes. However, the gaps between the bolts and the tubes still existed and a remarkable stiffness decrease might happen once the friction was overcome. Alternatively, self-drilling dowels (SDD) may provide a solution to address the challenges mentioned above. Fig. 1 shows one type of SDD as an example. SDD are made of hardened steel and available on market normally with 7-7.5 mm in diameter and up to 235 mm in length (Rothoblaas 2017; Rothoblaas 2019). With special self-peforating timber-metal tips, SDD can penetrate timber members and up to 10 mm thick steel plates without pre-drilling. Thus, SDD can eliminate the gaps between the fasteners and the holes and reduce considerable machining time for accurate drilling. Due to the fact that SDD are in small diameter and no pre-drilling is required, SDD connections can accommodate more fasteners in the joint areas and increase the number of shear planes by inserting two or three steel plates. The high slenderness of SDD also promotes dowel yielding mechanism. Thus, SDD connections have the potential to achieve higher strength and ductility when compared with connections with small amount of stocky bolts if brittle timber failures are avoided. Past research on SDD connections showed high initial stiffness, high load-carrying capacity and good ductility (Mischler 2001; Schreyer et al. 2004; Lau 2006; Dong and Li 2019), but none of the research was focused on moment connection applications. Therefore, there is a need to study the structural behaviour of moment connections with SDD.

To prevent brittle failure, a number of reinforcement methods have been developed, for example, by using fibre-reinforced plastics (Schober et al. 2015), densified veneer wood (Guan and Rodd 2001), plain round rods (He and Liu 2015), threaded rods (Dietsch and Brandner 2015), and self-tapping screws (STS) (Blaß and Bejtka 2005; Dietsch and Brandner 2015). Among them, STS have the economic advantages and are relatively easy to handle. Many experimental tests on dowel-type moment connections with STS reinforcement were conducted (Lam et al. 2010; Gehloff et al. 2010; Brühl et al. 2011; He and Liu 2015; He et al. 2016; Karagiannis et al. 2017; Zhang et al. 2019). All the tests showed that STS could enhance the connection strength and reduce the tendency of timber splitting, which shifted the brittle failure modes to more ductile ones including fastener bending

106 failure.

107 This paper aims to develop a good understanding of the rotational behaviour of glulam moment
108 connections with SDD by conducting an experimental and analytical study on full-scale connection
109 specimens. The effect of STS reinforcement on the connection performance is also investigated.
110 A modified analytical model (MAM) based on force and moment equilibrium is developed. For
111 model validation, the analytical predictions are compared to the experimental results and other
112 analytical models in literature.

113 EXPERIMENTAL TESTING

114 Materials and specimens

115 Seven full-scale beam-column moment connections were tested in the Structural Engineering
116 Laboratory at the University of Canterbury. The test matrix is listed in Table 1 and the specimen
117 design is shown in Fig. 2. All specimens had the same sizes and configurations of glulam beams and
118 columns, steel plates and SDD. The glulam beam and column cross sections were 450 mm×315 mm
119 and 315 mm×315 mm, respectively, and their average density and moisture contents were 466 kg/m^3
120 and 12%. Two 8 mm wide slots spaced at 88 mm were manufactured to accommodate two 6 mm
121 thick inserted steel plates. There were also 20 mm and 30 mm gaps around the steel plates in the
122 beam and column, respectively, for the installation convenience. The $\phi 7.5 \times 235$ SDD (Rothoblaas
123 2019) were used to drill through the glulam members and two inserted steel plates. All SDD were
124 over-driven by 36 mm to the glulam surfaces since the width of glulam members (315 mm) was
125 larger than the length of the SDD (235 mm). One connection specimen consisted of two joints, one
126 between the steel plates and the beam (referred as JPB) and the other between the steel plates and
127 the column (referred as JPC). JPC was considered as a more critical component in real buildings as
128 the failure of JPC may cause collapse of the column. Therefore, JPC was over-designed to remain
129 elastic before the failure of JPB.

130 Table 2 lists the dowel spacing in JPB and the relevant spacing requirements in Eurocode 5
131 (2004). The notations of spacing are shown in Fig. 3. Past research showed that the loaded edge
132 distance a_{4t} was the most critical factor for bolted moment connection (Lam et al. 2010) and a_{4t} in

Eurocode 5 (2004) seemed inadequate to prevent timber splitting for unreinforced glulam members. However, it will be more efficient for a moment connection to distribute the dowels far from the centroid of the dowel group, which means that smaller a_{4t} is preferred. As a compromise, increased a_{4t} to 50 mm was employed according to the timber rivet design guide (Zarnani and Quenneville 2013) as timber rivets have similar size with SDD and are widely used for moment connections in timber portal frames. The other spacing requirements are less critical, so increased a_1 and a_2 were used to spread out SDD for increased moment capacity. For STS-reinforced specimens (RSC group in Table 1), $\phi 8 \times 450$ STS (European Technical Approval 2017) with 5 mm pilot holes were installed as timber perpendicular-to-grain reinforcement. STS were positioned 25 mm away from the closest SDD to avoid a clash between STS and SDD within the glulam members. Because the STS were longer than the glulam column depth, the extra length of STS was cut off after the STS were installed in position. The mechanical properties of the materials used in the tests are listed in Table 3. The characteristic yield moment $M_{y,Rk}$ of SDD in Table 3 was derived from fifteen 3-point bending tests according to AS/NZS ISO 10984.1 (2015) and EN 14592 (2008).

The test setup is shown in Fig. 4. The specimens were rotated 90° to accommodate the horizontal loading system. The column was placed on two steel support plates and then anchored on the ground by two steel washer plates and four anchor bolts. Steel blocks were placed on both ends of the glulam column to restrain the horizontal movement. A horizontally placed actuator was attached to the top of the beam by a steel fitting. The actuator had a stroke range of ±250 mm and maximum load capacity of 400 kN. Beams in a moment frame may carry some axial loads. However, moment action typically governs the member and joint design for a timber moment frame. It was also found that axial forces inside beams had a small impact on the total moment capacity of beam-column connections (Shu et al. 2019). Therefore, the glulam beam was not axially loaded in this test setup.

Loading protocol and measurements

Displacement-control loading protocols were employed for both monotonic and cyclic tests. The specimen USM-1 in Table 1 was loaded monotonically to failure when the post-peak load dropped to 80% of the peak load as per EN 12512 (2002). All cyclic specimens (USC and

RSC groups in Table 1) followed the loading protocol in EN 12512 (2002) as well, which was 1 cycle at each of $0.25\Delta_{yr}$ and $0.5\Delta_{yr}$ amplitude followed by 3 cycles at $0.75\Delta_{yr}$, Δ_{yr}, $2\Delta_{yr}$ and $4\Delta_{yr}$ amplitude as shown in Fig. 5. The yield reference displacement Δ_{yr} was determined by the moment-displacement curve of USM-1 according to EN 12512 (2002), i.e. Δ_{yr} was the intersection of two lines. One line went through 10% and 40% of the maximum moment of the curve and the other line was the tangent line of the curve with one-sixth of the stiffness of the first line.

The applied load was measured by a load cell in the actuator. Potentiometers (P) and inclinometers (I) were installed to measure the connection movement. The instrumentation layout is shown in Fig. 4b. P1 was used to control the displacement of the actuator; P2 and P3 were fixed on both sides of the beam to monitor the twist of the specimen; P4 was used to measure the horizontal sliding of the specimen. I1-I4 and I5-I6 were installed to capture the rotation of the beam and column, respectively.

The movement of the inserted steel plates and the glulam members was expected to have translational and rotational components, which were very hard to decouple accurately by traditional instruments. Particle tracking technology (PTT), a contact-free measuring technique, has advantages over traditional instruments and was recently used in structural timber tests to capture crack growth of exposed timber surfaces in dowelled connections and compute the resulting displacement field (Ottenhaus et al. 2019). PTT was applied in this study to capture and decouple the complex movement between steel plates and glulam members. The inserted steel plates were deliberately oversized by 110 mm on both sides of the beam (Fig. 2) so that particles could be attached on the surface of the steel plates and the glulam members (Fig. 6 and Fig. 7). Digital cameras were used to capture the movement of particles at each loading step. Streams (Nokes 2017) was used to process the images taken by cameras and ultimately determine the coupled movement of the steel plates and the glulam members.

EXPERIMENTAL RESULTS AND DISCUSSION

Failure modes

For USM-1 under monotonic load, gap opening was observed and a longitudinal crack was initiated on the gap opening side of the connection when the connection rotation reached 1.2°. The load continued increasing and the crack continued propagating along the grain (Fig. 6a) and the width of the beam. The load dropped by more than 20% suddenly when the crack went through the whole width of the beam at 1.6° rotation. The timber splitting caused those SDD close to the beam edge to lose their embedment areas, which triggered the brittle failure of the connection. The failure modes of three USC specimens were similar to USM-1. After gap opening, timber splitting initiated on the gap opening side (Fig. 6b) with an average of 1.6° rotation and specimens gradually lost their strength. Then the crack propagated along the grain and two of USC specimens lost more than 20% of their strength after reaching 1.8° rotation. Timber splitting initiated and propagated on the other side as well at the same average rotations when the specimens were loaded along the other direction. Meanwhile, the width of the previous crack increased as shown in Fig. 6c. It was also noticed that the strength started to decrease before the first crack on the timber surface was observed. The reason could be that timber splitting or damage had occurred inside the timber beam before the crack on the timber surface initiated. At last, all timber splitting failures happened in the first $2\Delta_{yr}$ cycle.

The failure modes of RSC specimens were different with those of USM and USC specimens. The timber splitting failure on the gap opening side was prevented by STS. The connections reached peak load at an average rotation of 1.8° and thereafter, the load decreased slightly because SDD gradually reached their ultimate bending strength. A longitudinal crack was initiated on the opposite side of gap opening when the connection rotation reached an average rotation of 2.4° as shown in Fig. 7a. When the loading direction reversed, timber splitting also occurred on the other corner of the beam at the same average rotation, as shown in Fig. 7b. The corners of the beam had high compressive stresses, which caused high friction at the corners and perpendicular-to-grain wood crushing of the column. The timber splitting was due to the tensile stresses caused by high friction. Connection failure occurred at an average rotation of 3.7° due to the combination of

wood embedment crushing and low cycle fatigue failure of SDD as shown in Fig. 8. Fig. 8 also displays that some STS were touched and bent by SDD at the last test stage due to the large bending deformation of the SDD. Failures happened at the first $4\Delta_{yr}$ cycle due to more than 20% loss of maximum strength. STS proved to be effective to delay the timber splitting and allow more SDD to reach yielding strength, thus leading to a more ductile connection response.

Hysteresis curves

Fig. 9 shows the moment-rotation hysteresis curves of USC and RSC specimens. The rotation of the connections was measured by the inclinometers and the moment was calculated as the product of the applied load F_V and the distance H as shown in Fig. 4b. The three replicates in either USC or RSC group showed similar responses. Unlike typical bolted connections, no initial slips were observed in any specimen due to the tight fit between SDD and the holes.

USC specimens experienced sudden drop of load due to timber splitting. In particular, the moment of USC-1 and USC-2 dropped by more than 20%. Therefore, the ultimate rotation Δ_u for group USC was defined as the load drop point and the corresponding moment was defined as ultimate moment M_u. The stiffness of all RSC specimens decreased gradually beyond rotation of 0.8° and reached peak moment M_{peak} at an average rotation of 1.8°. The strength decreased to 80% of M_{peak} in the negative cycle with $4\Delta_{yr}$ magnitude. This occurred because the positive cycle with $4\Delta_{yr}$ magnitude had already caused fatigue failure of some SDD and impaired the connection capacity. The much lower capacity of the following two $4\Delta_{yr}$ cycles also reflected the failure of SDD. Therefore, Δ_u for RSC specimens was defined as the rotation when the load dropped to 80% of M_{peak} and the load at Δ_u was defined as M_u. The point that failure happened was marked in Fig. 9.

Fig. 10 shows the backbone curves of six specimens under cyclic loading as well as the monotonic curve of USM-1. The seven curves were very consistent before timber splitting happened. Table 4 summarizes the connection properties based on these curves following the definitions in EN 12512 (2002). M_{peak} is the maximum moment and the corresponding rotation is Δ_{peak}. The yield stiffness K_y is the slope of a straight line between 10% and 40% of M_{peak}. (Δ_y, M_y) is determined

from the intersection of the line and another line with slope of 1/6 K_y. The ductility factor μ is defined as Δ_u/Δ_y. It was found that Δ_y, M_y, K_y of RSC specimens were comparable to those of USC specimens. The differences were within 7% but the average M_{peak} and μ of RSC specimens were 14% and 164% higher than those of USC specimens, respectively. STS reinforcement slightly increased the moment capacity but significantly improved the connection ductility.

For comparison with the results of USC and RSC specimens, Table 5 summarizes the results of a series of glulam beam-column connection tests in literature. The SDD moment connections were significantly stronger and stiffer than most of the connections in literature due to the advantage of using more fasteners with small diameter and two inserted steel plates. Although the STS-reinforced specimens reported by Lam et al. (2010) achieved relatively high capacity, the connection rotation at yield moment was large (2.4°), which indicates a much lower rotational stiffness when compared with USC and RSC specimens. The test results reported by van Bakel et al. (2017) had comparable strength to USC and RSC specimens and even higher stiffness. However, those connections used densified veneer wood and expanded steel tubes, which are not readily available on the market and not as convenient to install as SDD.

Energy dissipation

Fig. 11 shows the cumulative energy dissipation of all six cyclic specimens. When compared to USC specimens, RSC specimens dissipated similar amount of energy at the first 8 cycles before yielding and slightly more energy from cycle 9 to cycle 11 as timber splitting happened earlier in USC specimens. After cycle 11, RSC specimens dissipated much more energy. USC and RSC specimens dissipated an average energy of 23.1 kJ and 31.6 kJ in the 14 total cycles, respectively. Apparently, STS reinforcement proved to be efficient to increase the energy dissipation capacity of the connections.

MODIFIED ANALYTICAL MODEL (MAM)

Several analytical models were proposed to predict the moment capacity of dowel-type connections. Based on Eurocode 5 (2004), Porteous and Kermani (2013) presented a design method in which the connection was assumed to rotate around the centroid of the fastener group and the

shear force was carried by all fasteners uniformly as shown in Fig. 12b and Fig. 12c. The point O is denoted as centre of rotation (CR). The analytical model from Zhang (2018) on reinforced moment connections used the same assumption for the location of CR. Furthermore, it was assumed that the reinforcement allowed the moment connections to reach the peak moment when the yielding of dowels occurred on three or four fastener areas. He et al. (2017) considered the moment contribution from the timber compression zone and the friction at the beam-column interface. Their tests on bolted connections indicated that CR was on the edge bolt line (L_{He} in Fig. 12a) and an analytical model was proposed to determine the location of CR by iterations. However, the analytical model was less conservative and overestimated M_{peak} by 12% – 23% when compared with the experimental tests. Shu et al. (2019) provided a simplified analytical model for bolted connections based on experimental tests and numerical modelling. The analytical model provided conservative predictions of moment capacity by neglecting the friction and assuming that CR was at the intersection of the edge bolt line and bottom line of the glulam beam (point O_{Shu} in Fig. 12a).

The above mentioned analytical models were used to predict the moment capacity of RSC specimens and the calculation process is attached in Appendix I. Table 6 lists the prediction results as well as the test results of RSC specimens. None of these models provided predictions for both M_y and M_{peak}. It was also found that the models by Porteous and Kermani (2013) and Zhang (2018) significantly underestimated the moment capacity. The possible reasons were that the contribution from the timber compression zone at the beam-column interface should not be neglected for small diameter fasteners (Leijten and Brandon 2013). The model by Shu et al. (2019) could not satisfy all equilibrium conditions for this type of SDD moment connections and using compression strength parallel to grain f_c to calculate the compression zone stress of the timber beam is questionable since the compression zone is more likely to be governed by the column's compression strength perpendicular to grain $f_{cp,0}$ as observed during tests. Therefore, these assumptions on the location of CR in literature might not be suitable for SDD moment connections.

Based on past research, the location of CR need to be reassessed. A modified analytical model (MAM) is presented here to calculate the trajectory of CR and to predict the moment capacity and

the corresponding rotation of SDD moment connections. A number of assumptions similar to the past analytical models are made in MAM:

1. The connection movement is dominated by rotation due to moment action;
2. The steel plates have negligible elastic deformation, thus rigid body motion is considered;
3. SDD have elastoplastic behaviour;
4. The stiffness of each fastener is irrelevant to the load-grain direction; and
5. Timber brittle failure is not considered.

The moment-rotation backbone curve of the SDD connections can be simplified as a trilinear model as shown in Fig. 13 since no initial slip existed. Three key points (Δ_y, M_y), $(\Delta_{peak}, M_{peak})$ and (Δ_u, M_u) are used to determine the curve. For USC specimens, MAM aims to predict their behaviour up to yield point (Δ_y, M_y). The post-yield behaviour is challenging to predict due to the sudden brittle timber splitting failure that is not included in the assumptions of MAM. However, for RSC specimens, timber splitting was delayed significantly. Thus, MAM can be used to further predict the post-peak behaviour. The derivation of MAM to calculate connection moment capacity and rotation as well as a verification of the assumed CR will be discussed in the following sections.

Connection moment capacity calculation

As mentioned in the specimen design, JPC was over designed, so the capacity of the connection was governed by JPB. The load action on the beam is shown in Fig. 14. A global coordinate system XOY is established with the origin at the centroid of fastener group (point O). The fastener rows and columns are numbered (m rows and n columns). F_{ij} represents the force carried by the individual SDD at row i and column j (denoted as SDD_{ij}). The applied load F_V is exerted on the top of the beam, which causes F_{ij}, the compression force F_N and the friction force F_R at the bottom of the beam. At each load step, there is a CR, labelled as point O', which all SDD rotate around. Point O' must be within quadrant III of the global coordinate system XOY (shaded area in Fig. 14) to satisfy the force and moment equilibrium. A local coordinate system $X'O'Y'$ is established at point O' and the distance between point O' and SDD_{ij} is r'_{ij} which is perpendicular to F_{ij}. Therefore, the

force equilibrium of the beam along the X' and Y' directions and the moment equilibrium around point O' can be expressed by Eq. (1):

$$F_{B,X'} = \sum_{i=1,j=1}^{i=m,j=n} F_{ij,X'} = -F_N \tag{1a}$$

$$F_{B,Y'} = \sum_{i=1,j=1}^{i=m,j=n} F_{ij,Y'} = F_V + F_R \tag{1b}$$

$$M_{B,O'} = \sum_{i=1,j=1}^{i=m,j=n} F_{ij} r'_{ij} = F_V(H - l_R) - F_R l_R - F_N l_N \tag{1c}$$

with:

$$F_{ij,X'} = -\frac{F_{ij,max}}{r'_{max}} y'_{ij} \tag{2a}$$

$$F_{ij,Y'} = \frac{F_{ij,max}}{r'_{max}} x'_{ij} \tag{2b}$$

$$F_N = \begin{cases} \frac{1}{2} f_{cp} d_c b & if\ F_N \le \frac{1}{2} f_{cp,0} d_c b \\ f_{cp,0}(1-\beta) d_c b + \frac{1}{2} f_{cp,0} \beta d_c b & if\ F_N > \frac{1}{2} f_{cp,0} d_c b \end{cases} \tag{3}$$

$$F_R = \mu_f F_N \tag{4}$$

$$l_R = l_{O,X} + x_B \tag{5a}$$

$$l_N = \begin{cases} \frac{2}{3}d_c & if\ F_N \le \frac{1}{2}f_{cp,0}d_c b \\ \frac{3-\beta^2}{6-3\beta}d_c & if\ F_N > \frac{1}{2}f_{cp,0}d_c b \end{cases} \tag{5b}$$

$$d_c = l_{O,Y} + y_B \tag{5c}$$

where,

$F_{B,X'}$ and $F_{B,Y'}$ are the total force of the fastener group of JPB in the X' and Y' direction, respectively;

$M_{B,O'}$ is the total moment of the fastener group of JPB around point O' (positive in the anticlockwise direction);

$F_{ij,X'}$ and $F_{ij,Y'}$ are the components of individual F_{ij} in the X' and Y' direction, respectively;

H is the distance between F_V and the beam end;

l_R is the distance between point O' and the beam end;

l_N is the distance between point O' and the centroid of F_N;

$F_{ij,max}$ and r'_{max} are the maximum force and maximum distance among SDD_{ij} in the local coordinate system $X'O'Y'$;

(x'_{ij}, y'_{ij}) is the coordinate of SDD_{ij} in the local coordinate system $X'O'Y'$;

(x_B, y_B) is the coordinate of point O' in the global coordinate system XOY;

d_c is the length of compression zone;

b is the net width of the beam;

f_{cp} is the maximum compressive stress at the beam column interface;

β is the ratio of the linear portion length to d_c;

$\mu_f = 0.2$ is the coefficient of friction; and

$l_{O,X}$ and $l_{O,Y}$ are the distances between the corner of the beam and point O in the X and Y direction.

Because no column crushing was observed before the load reached M_y during the tests, the triangular stress distribution from the column was assumed as shown in scenario (a) of Fig. 14. $M_{B,O'}$ can be expressed as Eq. (6) by substituting Eq. (1a) and Eq. (1b) into Eq. (1c). Then, by rewriting Eq. (6), the trajectory equation $T_{CR,y}$ of (x_B,y_B) before the connection yielding can be expressed as Eq. (7).

$$M_{B,O'} = (F_{B,Y'} + \mu_f F_{B,X'})(H - l_{O,X} - x_B) + \mu_f F_{B,X'}(l_{O,X} + x_B) + \frac{2}{3}F_{B,X'}(l_{O,Y} + y_B) \tag{6}$$

$$y_B = \frac{3}{2}\frac{F_{B,Y'}}{F_{B,X'}}x_B - \frac{3}{2}(H - l_{O,X})\frac{F_{B,Y'}}{F_{B,X'}} - \frac{3}{2}(\mu_f H + \frac{2}{3}l_{O,Y}) + \frac{3}{2}\frac{M_{B,O'}}{F_{B,X'}} \tag{7}$$

If the fastener patterns are biaxially symmetric as the ones are in the tests, it can be derived that:

$$\sum_{i=1,j=1}^{i=m,j=n} x_{ij} = 0 \tag{8a}$$

$$\sum_{i=1,j=1}^{i=m,j=n} y_{ij} = 0 \tag{8b}$$

where, (x_{ij}, y_{ij}) is the coordinate of SDD_{ij} in the global coordinate system XOY.

According to Eq. (2) and Eq. (8), it can be derived that:

$$\frac{F_{B,Y'}}{F_{B,X'}} = \frac{\sum F_{ij,Y'}}{\sum F_{ij,X'}} = -\frac{\sum x'_{ij}}{\sum y'_{ij}} = -\frac{\sum(x_{ij} - x_B)}{\sum(y_{ij} - y_B)} = -\frac{x_B}{y_B} \tag{9a}$$

$$M_{B,O'} = \sum F_{ij} r'_{ij} = \frac{\sum(x'^2_{ij} + y'^2_{ij})}{r'_{max}} F_{ij,max} \tag{9b}$$

$$\frac{M_{B,O'}}{F_{B,X'}} = -\frac{\sum(x'^2_{ij} + y'^2_{ij})}{\sum y'_{ij}} = -\frac{\sum[(x_{ij} - x_B)^2 + (y_{ij} - y_B)^2]}{\sum(y_{ij} - y_B)} = \frac{\sum(x^2_{ij} + y^2_{ij})}{n_{sd} y_B} + \frac{x_B^2}{y_B} + y_B \tag{9c}$$

where, n_{sd} is the number of SDD in the JPB.

Therefore, $T_{CR,y}$ can be simplified as Eq. (10) by substituting Eq. (9) into Eq. (7). Eq. (10) shows that $T_{CR,y}$ is a parabolic function dependent on the configuration of fastener group, H and μ_f.

$$y_B^2 + 3(H - l_{O,X})x_B - (3\mu_f H + 2L_{O,Y})y_B + \frac{3J_O}{n_{sd}} = 0 \tag{10}$$

with:

$$J_O = \sum (x_{ij}^2 + y_{ij}^2) \tag{11}$$

Using the connection information of USC and RSC, $T_{CR,y}$ can be expressed as Eq. (12) and plotted in Fig. 15. The predicted M_y is reached by meeting two criteria: (1) the farthest SDD to point O' reaches its characteristic strength $F_{v,Rk}$, and (2) The timber crushing of the column is about to occur ($f_{cp} = f_{cp,0}$).

$$x_B = -\frac{1}{3240}y_B^2 + \frac{67}{180}y_B - 25.88 \tag{12}$$

The SDD connection with two inserted steel plates can be modelled as the superposition of two simple joints (J1 and J2) shown in Fig. 16 and calculated by Eq. (13) based on the research by Fan et al. (2011). The strength of J1 and J2 can be calculated by Eq. (14) and Eq. (15), respectively, according to Eurocode 5 (2004). The capacity of J2 should be interpolated between Eq. (15a) and Eq. (15b) as the steel plate thickness is between thin and thick steel plate definitions in Eurocode 5 (2004). The effective number of dowels n_{ef} has not been considered in this model as the fasteners are loaded in different directions in a moment connection.

$$F_{v,Rk} = n_{J1}F_{J1} + n_{J2}F_{J2}; \tag{13}$$

366 with:

$$F_{J1} = min \begin{cases} f_{h,A,k} t_A d \\ f_{h,A,k} t_A d \left[\sqrt{2 + \frac{4 M_{y,Rk}}{f_{h,A,k} d t_A^2}} - 1 \right] \\ 2.3 \sqrt{M_{y,Rk} f_{h,A,k} d} \end{cases} \tag{14}$$

$$F_{J2,1} = min \begin{cases} 0.5 f_{h,B,k} t_B d \\ 1.15 \sqrt{2 M_{y,Rk} f_{h,B,k} d} \end{cases} \tag{15a}$$

$$F_{J2,2} = min \begin{cases} 0.5 f_{h,B,k} t_B d \\ 2.3 \sqrt{M_{y,Rk} f_{h,B,k} d} \end{cases} \tag{15b}$$

$$f_{h,\alpha,k} = \frac{f_{h,0,k}}{k_{90} \sin^2 \alpha + \cos^2 \alpha} \tag{16a}$$

$$f_{h,0,k} = 0.082(1 - 0.01d)\rho_k \tag{16b}$$

$$k_{90} = 1.35 + 0.015d \tag{16c}$$

367 where,

368 $F_{v,Rk}$ is the characteristic strength per SDD;

369 F_{J1} is the characteristic strength per shear plane for J1;

370 $F_{J2,1}$ and $F_{J2,2}$ are characteristic strength per shear plane for connection with thin and thick
371 steel side plate, respectively;

372 $n_{J1} = 2$ and $n_{J2} = 2$ are the shear plane number of J1 and J2, respectively;

373 $f_{h,A,k}$ and $f_{h,B,k}$ are the characteristic embedment strength of layer A and layer B, respec-
374 tively;

375 t_A is the penetration depth of SDD in layer A;

376 t_B is the thickness of layer B;

377 d is the diameter of SDD;

α is the angle of the load to the grain; and

$\rho_k = 434\,\text{kg/m}^3$ is the characteristic density of the glulam members in this study.

The search for the coordinates O' $(x_B,\ y_B)$ associated with M_y along $T_{CR,y}$, labelled as O'_y, follows a flowchart in Fig. 17. It is a convenient search by spreadsheets. For USC and RSC specimens, the coordinate of point O'_y turned out to be (−60 mm,−85 mm) and predicted M_y was $91.8\,\text{kN}\cdot\text{m}$.

The predicted M_{peak} is reached when the maximum amounts of SDD reach their characteristic strength and compression zone of the column does not exceed full plastic capacity ($\beta \geq 0$). The predicted M_u is defined as 80% of predicted M_{peak}. The similar process mentioned above can be used to calculate the trajectory at M_{peak} (denoted as $T_{CR,peak}$). However, $T_{CR,peak}$ is more complicated since more SDD have yielded, which transfers Eq. (2) to Eq. (17). $T_{CR,peak}$ cannot be simplified as before and complex iterations (He et al. 2017) are required to locate CR at M_{peak} (denoted as point O'_{peak}). It was observed from RSC testing that the applied load F_V increased slightly but the rotation increased significantly after M_y, which meant that $F_{ij,Y'}$ in Eq. (17b) did not change significantly. To avoid complex iterations, it was assumed that y_B continued to decrease but x_B kept constant after M_y, and the increase of F_V was primarily from the gradual yielding of SDD. Therefore, $T_{CR,peak}$ can be simplified as a vertical line shown in Fig. 15. By a search method following the flowchart in Fig. 17, the location of point O'_{peak} can be found quickly by spreadsheets. The results showed that the coordinate of point O'_{peak} was (−60 mm,−108 mm) and the predicted M_{peak} was $124.4\,\text{kN}\cdot\text{m}$. The calculation also showed that SDD in row 1 and row 2 of Fig. 14 reached their characteristic strength with $\beta = 0.64$ at predicted M_{peak}. The predictions by iterations were (−68 mm,−128 mm) for point O'_{peak} and $126.2\,\text{kN}\cdot\text{m}$ for M_{peak}, which presented that the simplification of $T_{CR,peak}$ was reasonable with 1% error on moment capacity.

$$F_{ij,X'} = \begin{cases} -\frac{F_{v,Rk}}{r'_{ij}} y'_{ij} = -\frac{F_{v,Rk}}{r'_{ij}} (y_{ij} - y_B) & r'_{ij} > r'_D \\ -\frac{F_{v,Rk}}{r'_D} y'_{ij} = -\frac{F_{v,Rk}}{r'_D} (y_{ij} - y_B) & r'_{ij} \leq r'_D \end{cases} \tag{17a}$$

$$F_{ij,Y'} = \begin{cases} \frac{F_{v,Rk}}{r'_{ij}} x'_{ij} = \frac{F_{v,Rk}}{r'_{ij}} (x_{ij} - x_B) & r'_{ij} > r'_D \\ \frac{F_{v,Rk}}{r'_D} x'_{ij} = \frac{F_{v,Rk}}{r'_D} (x_{ij} - x_B) & r'_{ij} \leq r'_D \end{cases} \tag{17b}$$

where, r'_D is the minimum distance between point O'_{peak} and the SDD that have reached $F_{v,Rk}$.

The MAM predicted M_y was 91.8 kN · m, 20% higher than 76.7 kN · m following the method by Porteous and Kermani (2013), and the predicted M_{peak} was 124.4 kN · m, 41% higher than 88.5 kN · m following the method by Zhang (2018). However, the predicted M_y and M_{peak} by MAM were still 29% and 17% lower than the average test results of RSC specimens. The reasons could be that more than one SDD reached characteristic strength at M_y during tests and that the characteristic material properties were used in the prediction, which tended to predict the lower boundary of connection strength.

Connection rotation calculation

The rotation of the beam-column connections has two components, the rotation of JPB Δ_B and the rotation of JPC Δ_C as shown in Fig. 18. Δ_B can be calculated by Eq. (18) and the SDD group stiffness of JPB K_B depends on the fastener stiffness. Two methods were used in this study to predict the fastener stiffness. The first one was the stiffness at ultimate limit state (ULS) $k_{u,1}$ for per shear plane per fastener as shown in Eq. (20) according to Eurocode 5 (2004). The other method shown in Eq. (21) was the test-based stiffness $k_{u,2}$ from SDD connection tests (Dong and Li 2019) and SDD 3-point bending tests. In those tests, SDD reached $M_{y,Rk}$ at an average deformation of 2.5 mm. The stiffness results of JPB are listed in Table 7.

$$\Delta_{B,y} = M_{B,O',y}/K_{B,y} \tag{18a}$$

$$\Delta_{B,peak} = \Delta_{B,y} + (M_{B,O',peak} - M_{B,O',y})/K_{B,peak} \tag{18b}$$

418 with:

$$K_B = (n_{J1} + n_{J2})k_u \sum_{i=1,j=1}^{i=m,j=n} r_{ij}'^2 \tag{19a}$$

$$k_u = \begin{cases} k_{u,1} \text{ or } k_{u,2} & F_{ij} < F_{v,Rk} \\ 0 & F_{ij} = F_{v,Rk} \end{cases} \tag{19b}$$

$$k_{ser} = k_{mat}\frac{\rho_m^{1.5} d}{23} \tag{20a}$$

$$k_{u,1} = \frac{2}{3}k_{ser} \tag{20b}$$

$$k_{u,2} = \frac{F_{v,Rk}}{\delta_y(n_{J1} + n_{J2})} \tag{21}$$

419 where,

420 $M_{B,O',y}$ and $M_{B,O',peak}$ are the moment resistance of JPB at the predicted M_y and M_{peak},
421 respectively;

422 $K_{B,y}$ and $K_{B,peak}$ are the SDD group stiffness of JPB at the predicted M_y and M_{peak},
423 respectively;

424 k_u is the fastener stiffness;

425 $k_{mat} = 2$ is the modification factor for timber-to-steel connection;

426 $\rho_m = 466\,\text{kg/m}^3$ is the mean density of glulam members in this study; and

427 $\delta_y = 2.5\,\text{mm}$ is the yield deformation of SDD.

The load action in the inserted steel plate is shown in Fig. 19. $F_{B,X'}$, $F_{B,Y'}$ and $M_{B,O'}$ are the loads from JPB. The location of CR in JPC, labelled as point O'', can be estimated by the same method with JPB. However, because JPC is over designed to remain elastic, close enough prediction results can be obtained by assuming point O'' at the centroid of its fastener group. A local coordinate system $X''O''Y''$ is established and the forces and moment carried by JPC ($F_{C,X''}$, $F_{C,Y''}$ and $M_{C,O''}$) can be calculated by Eq. (22). Consequently, Δ_C can be predicted by Eq. (23). As JPC is over-designed to remain elastic, only its elastic group stiffness K_C is listed in Table 7.

$$F_{C,X''} = F_{B,X'} \tag{22a}$$

$$F_{C,Y''} = F_{B,Y'} \tag{22b}$$

$$M_{C,O''} = M_{B,O'} - F_{B,X'}y'_C - F_{B,Y'}x'_C \tag{22c}$$

where, $F_{C,X''}$ and $F_{C,Y''}$ are the total forces of fastener group of JPC in the X'' and Y'' direction, respectively; $M_{C,O''}$ is the total moment of fastener group of JPC around point O''; (x'_C,y'_C) is the coordinate of point O'' in the local coordinate system $X'O'Y'$.

$$\Delta_C = M_{C,O''}/K_C \tag{23}$$

with:

$$K_C = (n_{J1} + n_{J2})k_u \sum_{i=1,j=1}^{i=p,j=q} r''^2_{ij} \tag{24}$$

where, K_C is the SDD group stiffness of JPC; r''_{ij} is the distance between point O'' and SDD_{ij} in JPC in the local coordinate $X''O''Y''$.

At post-peak stage of RSC specimens, the rotation of JPB continued increasing but the moment capacity decreased slowly due to the gradual low cycle fatigue failure of SDD at the edge row. It was conservative to consider the ultimate rotation of JPB $\Delta_{B,u}$ as the rotation when the earliest yielded SDD reached its ultimate deformation δ_f and broke. It was assumed that the beam continued

rotating around point O'_{peak}. The tests of RSC specimens showed that SDD failed at a average deformation of 18 mm (Fig. 8). Therefore, $\Delta_{B,u}$ can be calculated by Eq. (25) in MAM.

$$\Delta_{B,u} = \delta_f / r'_{1n} \tag{25}$$

where, $\delta_f = 18$ mm is the ultimate deformation of SDD; r'_{1n} is the maximum distance between all SDD and point O'_{peak} as shown in Fig. 14.

Table 8 summarizes the rotation predictions and the average experimental results of RSC specimens. Fig. 20 shows the backbone curves of RSC specimens and the trilinear backbone curves predicted by MAM. It was found that the backbone curve based on Eurocode 5 (2004) overestimated the stiffness of the connections and caused less conservative results, while the backbone curves based on 3-point bending tests provided conservative predictions. The reason that $k_{u,1}$ overestimated the fastener stiffness of SDD could be that the modification factor $k_{mat} = 2.0$ in Eurocode 5 (2004) was not appropriate for the SDD moment connection, since the holes in the steel plates could have bearing deformation considering the plates were relatively thin to facilitate the self-drilling. Therefore, it is recommended to take k_{mat} as 1.5 or 1.0 conservatively as suggested by Wang et al. (2020) and Dong et al. (2020) for the SDD moment connections to consider the factors that are not included in Eq. (20a) such as the slenderness of dowels (Lemaître et al. 2018). In addition, 3-point bending tests can be used to achieve a more accurate estimation of the fastener stiffness for timber-to-steel dowel-type connections with slender fasteners. Table 8 shows that the analytical rotation Δ_{an} based on $k_{u,2}$ is slightly smaller than the average experimental results Δ_{ex}. One reason could be that the SDD still required a small displacement to fully engage and reach maximum stiffness (Dorn 2012). The other reason could be that the bending deformation of the beam and column was neglected.

Verification on the centre of rotation

The movement of the beam and the steel plate was tracked by PTT in the testing. Their relative movement, i.e. individual SDD slip could be derived. Using RSC-1 as an example, Fig. 21 shows

the slip trajectory of SDD_{11} to SDD_{15} numbered in Fig. 14. Fig. 21 illustrates that JPB had different vertical movement at the position of SDD_{11} and SDD_{13}, so the x-coordinate of CR should be located between these two points. In this manner, CR at M_y and M_{peak} during tests were estimated. The average location of CR for three RSC specimens based on the PTT measurements are marked in Fig. 22 as well as the predicted location of CR by MAM. The results show that the MAM provided a good agreement with the test results with an average difference of 17.4 mm. Therefore, CR from MAM is verified and can be used to predict the connections' moment capacity and rotation.

CONCLUSIONS

Experimental testing of seven full-scale glulam beam-column moment connections with self-drilling dowels (SDD) was conducted. The influence of self-tapping screw (STS) reinforcement on the connection performance was also investigated. A modified analytical model (MAM) was proposed based on force and moment equilibrium of glulam members. The main research findings are listed as follows:

- All SDD moment connections achieved high initial stiffness and high moment capacity when compared with the test results of bolted connections reported in literature. SDD helped to eliminate the gaps between the fasteners and the oversized holes, which are generally required in bolted connections. SDD could also accommodate double inserted steel plates without strict tolerance control.
- The brittle timber splitting failure occurred on the unreinforced specimens (USM and USC) despite the increased edge distance. The STS-reinforced specimens (RSC) had average 14% higher maximum moment capacity (149.4 kN · m vs. 130.7 kN · m) and 164% higher ductility (4.5 vs. 1.7) when compared with USC specimens. The STS reinforcement effectively reduced timber splitting tendency and encouraged full yielding of more SDD. It is recommended to reinforce SDD moment connections, for example, by self-tapping screws for enhanced performance.
- The existing analytical models with the assumptions on centre of rotation (CR) of the

fastener group did not provide accurate predictions for the SDD moment connections. The proposed MAM provided a convenient method to predict the location of CR by spreadsheets, which improved the prediction accuracy of moment capacity. MAM was able to predict the SDD connection behaviour before yielding for both USC and RSC specimens, and the post-yield behaviour for RSC specimens.

- The stiffness prediction based on Eurocode 5 overestimated the connection stiffness by 36% when the modification factor of 2.0 for timber-to-steel connections was used. A more conservative modification factor of 1.5 or 1.0 was recommended for the SDD moment connections. The 3-point bending tests for fasteners were also proved to be an effective method to predict the stiffness for the SDD connections.

DATA AVAILABILITY STATEMENT

- Some or all data, models, or code that support the findings of this study are available from the corresponding author upon reasonable request.

ACKNOWLEDGEMENTS

The authors would like to thank QuakeCore, the Natural Hazards Research Platform in New Zealand, University of Canterbury, Techlam and Timber Connect Limited for partially sponsoring the project. The authors appreciate the technical support provided by Prof. Roger Nokes, technicians Russell McConchie, Alan Thirlwell, Michael Weavers and Dave Carney from the University of Canterbury.

APPENDIX I. MOMENT CAPACITY CALCULATION PROCESS IN THE PAST ANALYTICAL MODELS

Model from Porteous and Kermani (2013)

The following assumptions were made for the model by Porteous and Kermani (2013):

1. The position of the centre of rotation (CR) of the fasteners in the connection remains fixed;
2. The CR is at the geometric center of the fastener group when the fasteners are all the same size;
3. Each fastener will take an equal shear of the lateral load;
4. The stiffness of each fastener is irrelevant to the load-grain direction; and
5. Timber brittle failure is prevented by satisfying the spacing and end and edge distance requirements in Eurocode 5 (2004).

The CR is assumed at point O as shown in Fig. 23 for JPB. Each fastener carries F_{ij} the fastener load caused by the moment M_0, and $F_{ij,v}$ the fastener load caused by the shear force F_V. The equilibrium is shown in Eq. (26)-Eq. (27). The combined load $F_{ij,com}$ and its corresponding angle to timber grain θ_{ij} are calculated by Eq. (28). The limit state is assumed when the maximum $F_{ij,com}$ in the fastener group (SDD_{15} and SDD_{55} in this example) reaches the fastener's characteristic value $F_{v,Rk}$ at θ_{15} and θ_{55} (31.7 kN with $\theta_{15} = \theta_{55} = 35.7°$). The predicted yield moment of JPB, M_y is 76.6 kN · m as the product of the F_V and H as shown in Fig. 23.

$$M_O = F_V(H - l_{O,X}) = \sum_{i=1,j=1}^{i=5,j=5} F_{ij} r_{ij} \tag{26a}$$

$$F_V = \sum_{i=1,j=1}^{i=5,j=5} F_{ij,v} = n_{sd} F_{ij,v} \tag{26b}$$

with:

$$F_{ij} = \frac{F_{ij,max}}{r_{max}} r_{ij} \tag{27a}$$

$$F_{ij,X} = -\frac{F_{ij,max}}{r_{max}} y_{ij} \tag{27b}$$

$$F_{ij,Y} = \frac{F_{ij,max}}{r_{max}} x_{ij} \tag{27c}$$

$$F_{ij,com} = \sqrt{(F_{ij,X})^2 + (F_{ij,Y} + F_{ij,v})^2} \leq F_{v,Rk} \text{ at } \theta_{ij} \tag{28a}$$

$$\theta_{ij} = \left| \arctan \frac{F_{ij,Y} + F_{ij,v}}{F_{ij,X}} \right| \tag{28b}$$

Model from Zhang (2018)

The model from Zhang (2018) was further developed based on the model from Porteous and Kermani (2013) to predict the maximum moment capacity M_{peak}. Therefore, the same assumptions with the model from Porteous and Kermani (2013) are applied. In addition, because all specimens were reinforced by partially threaded screws perpendicular to timber grain to avoid brittle failure, another assumption is made that the connection is effective until failure has occurred to three or four fastener areas and the failed areas continue to provide their full load-carrying capacity and support to vertical load until the total number of failed areas reaches to three or four.

In this example, SDD_{15} and SDD_{55} are the first two failed areas and their force F_{15} and F_{55} can be obtained as 29.6 kN based on analytical model from Porteous and Kermani (2013). The loads of the first two failed areas will keep constant until ultimate state of the connection has reached. In this example, the third and fourth failed areas will occur together according to symmetry of fastener layouts and the corresponding moment ($M = F_V H$) is the predicted peak moment M_{peak}. There are two options for potential failed areas: 1) SDD_{11} and SDD_{51}; 2) SDD_{25} and SDD_{45}. These two options will be calculated by Eq. (29)-Eq. (30). The limit state is assumed when either the combined load $F_{11,com}$ or $F_{25,com}$ calculated by Eq. (28) reaches the fastener's characteristic value

$F_{v,Rk}$ at θ_{11} and θ_{25} for two options, respectively. M_{peak} is 88.5 kN · m for option 1 and 97.2 kN · m for option 2. Therefore, the moment capacity is governed by option 1 and M_{peak} is 88.5 kN · m.

$$M_O = F_V(H - l_{O,X}) = \sum F_{ij} r_{ij} + F_{15} r_{15} + F_{55} r_{55} \tag{29a}$$

$$F_V = \sum_{i=1,j=1}^{i=5,j=5} F_{ij,v} = n_{sd} F_{ij,v} \tag{29b}$$

with:

$$F_{ij} = \begin{cases} \frac{F_{11}}{r_{11}} r_{ij} & \text{option 1} \\ \frac{F_{25}}{r_{25}} r_{ij} & \text{option 2} \end{cases} \tag{30a}$$

$$F_{ij,X} = \begin{cases} -\frac{F_{11}}{r_{11}} y_{ij} & \text{option 1} \\ -\frac{F_{25}}{r_{25}} y_{ij} & \text{option 2} \end{cases} \tag{30b}$$

$$F_{ij,Y} = \begin{cases} \frac{F_{11}}{r_{11}} x_{ij} & \text{option 1} \\ \frac{F_{25}}{r_{25}} x_{ij} & \text{option 2} \end{cases} \tag{30c}$$

Model from Shu et al. (2019)

In this model, an assumption is made that the CR of JPB is always at intersection of the column surface and edge fastener line (point O' in Fig. 24). In addition, the friction force is not considered. The load action for JPB is shown in Fig. 24 and the predicted peak moment M_{peak} is calculated by either Eq. (31a) or Eq. (31b) according to equilibrium Eq. (32). The limit state is reached when the farthest fastener to point O' (SDD_{15} in this example) reaches its characteristic strength $F_{v,Rk}$ (31.4 kN with the angle to timber grain $\theta'_{15} = 38.7°$). For JPB, d_c, β, b are 50 mm, 0.77 and 299 mm, respectively, resulting in $M_{peak,1}$ =110.9 kN · m and $M_{peak,2}$ =254.1 kN · m. It is noticed that there is a significant difference between $M_{peak,1}$ and $M_{peak,2}$. The reason is that the CR assumption enforces the force equilibrium (Eq. (1a) Eq. (1b)) but cannot satisfy the moment equilibrium (Eq. (1c)). In addition, using compression strength parallel to grain f_c in Eq. (32e) is

561 questionable since the compression zone contribution is more likely to be governed by the column's
562 compression strength perpendicular to grain $f_{cp,0}$ as observed from the tests.

$$M_{peak,1} = M_{B,O'} + \alpha_{BC} F_N l_N \tag{31a}$$

$$M_{peak,2} = F_V H \tag{31b}$$

with:

$$M_{B,O'} = \sum_{i=1,j=1}^{i=5,j=5} F_{ij} r'_{ij} \tag{32a}$$

$$F_{ij} = \frac{F_{ij,max}}{r'_{max}} r'_{ij} \tag{32b}$$

$$\alpha_{BC} = 3^{(2-\frac{d}{4})} \tag{32c}$$

$$F_N = \sum_{i=1,j=1}^{i=5,j=5} F_{ij,X'} \tag{32d}$$

$$l_N = \begin{cases} \frac{2}{3} d_c & if\ F_N \leq \frac{1}{2} f_c d_c b \\ \frac{3-\beta^2}{6-3\beta} d_c & if\ F_N > \frac{1}{2} f_c d_c b \end{cases} \tag{32e}$$

$$F_V = \sum_{i=1,j=1}^{i=5,j=5} F_{ij,Y'} \tag{32f}$$

REFERENCES

Australian/New Zealand Standard (2015). "AS/NZS ISO 10984.1:2015 (2015) Timber structures—dowel-type fasteners—determination of yield moment." *Report no.*, Sydney, Australia/ Wellington, New Zealand.

Awaludin, A., Smittakorn, W., Hayashikawa, T., and Hirai, T. (2007). "M-θ curve of timber connection with various bolt arrangements under monotonic loading." *Journal of Structural Engineering, A*, 53, 853–862.

Blaß, H. J. and Bejtka, I. (2005). "Self-tapping Screws as Reinforcements in Connections with Dowel-type Fasteners." *Working commission W18 on Timber structures*, (August), 19.

British Standard Institution (BSI) (2002). "BS EN 12512:2001: Timber structures. Test methods. Cyclic testing of joints made with mechanical fasteners.

British Standard Institution (BSI) (2004). "Eurocode 5: design of timber structures—Part 1-1: General—Common rules and rules for buildings.

British Standard Institution (BSI) (2008). "EN 14592: Timber structures - Dowel-type fasteners - Requirements.

Brühl, F., Kuhlmann, U., and Jorissen, A. (2011). "Consideration of plasticity within the design of timber structures due to connection ductility." *Engineering Structures*, 33(11), 3007–3017.

Buchanan, A. H. and Fairweather, R. H. (1993). "Seismic design of glulam structures." *Bulletin of the New Zealand National Society for Earthquake Engineering*, 26(4), 415–436.

Di Cesare, A., Ponzo, F. C., Nigro, D., Pampanin, S., and Smith, T. (2017). "Shaking table testing of post-tensioned timber frame building with passive energy dissipation systems." *Bulletin of Earthquake Engineering*, 15(10), 4475–4498.

Dietsch, P. and Brandner, R. (2015). "Self-tapping screws and threaded rods as reinforcement for structural timber elements-A state-of-the-art report." *Construction and Building Materials*, 97, 78–89.

Dong, W. and Li, M. (2019). "A preliminary study on cyclic behaviour of SFS dowelled connections in glulam frames." *11th Pacific Conference on Earthquake Engineering*, Auckland, New Zealand,

paper 105.

Dong, W., Li, M., Lee, C.-l., Macrae, G., and Abu, A. (2020). "Experimental testing of full-scale glulam frames with buckling restrained braces." *Engineering Structures*, 222(March), 111081.

Dorn, M. (2012). "Investigations on the Serviceability Limit State of Dowel-Type Timber Connections." Doctoral thesis, Vienna University of Technology,

European Technical Approval (2017). "SPAX International GmbH & Co. KG: Self-tapping screws for use in timber constructions ETA-17/0114." *Report no.*, ETA-Denmark.

Fan, X., Zhang, S., and Qu, W. (2011). "Load-carrying behaviour of dowel-type timber connections with multiple slotted-in steel plates." *Applied Mechanics and Materials*, 94-96, 43–47.

Fragiacomo, M. and Batchelar, M. (2012). "Timber frame moment joints with glued-in steel rods. II: Experimental investigation of long-term performance." *Journal of Structural Engineering (United States)*, 138(6), 802–811.

Gehloff, M., Closen, M., and Lam, F. (2010). "Reduced edge distances in bolted timber moment connections with perpendicular to grain reinforcements." *11th World Conference on Timber Engineering 2010, WCTE 2010*, 2(December), 970–977.

Gilbert, C. F. and Erochko, J. (2019). "Development and testing of hybrid timber-steel braced frames." *Engineering Structures*, 198(July).

Granello, G., Palermo, A., Pampanin, S., Pei, S., and Van De Lindt, J. (2020). "Pres-Lam Buildings: State-of-the-Art." *Journal of Structural Engineering (United States)*, 146(6), 1–16.

Granello, G., Palermo, A., Pampanin, S., Smith, T., and Sarti, F. (2018). "The implications of post-tensioning losses on the seismic response of pres-lam frames." *Bulletin of the New Zealand Society for Earthquake Engineering*, 51(2), 57–69.

Guan, B. Z. and Rodd, P. (2001). "DVW—Local reinforcement for timber joints." *Journal of structural engineering*, 127(8), 894–900.

He, M., Zhang, J., and Li, Z. (2017). "Influence of cracks on the mechanical performance of dowel type glulam bolted joints." *Construction and Building Materials*, 153, 445–458.

He, M., Zhao, Y., and Ma, R. (2016). "Experimental investigation on lateral performance of pre-

617 stressed tube bolted connection with high initial stiffness." *Advances in Structural Engineering*,
618 19(5), 762–776.
619 He, M. J. and Liu, H. F. (2015). "Comparison of glulam post-to-beam connections reinforced by
620 two different dowel-type fasteners." *Construction and Building Materials*, 99, 99–108.
621 Iqbal, A., Pampanin, S., and Buchanan, A. H. (2016). "Seismic performance of full-scale post-
622 tensioned timber beam-column connections." *Journal of Earthquake Engineering*, 20(3), 383–
623 405.
624 Johansen, K. W. (1949). "Theory of timber connections." *Int Assoc Bridge Struct Eng*, 9, 249–262.
625 Karagiannis, V., Málaga-Chuquitaype, C., and Elghazouli, A. Y. (2017). "Behaviour of hybrid
626 timber beam-to-tubular steel column moment connections." *Engineering Structures*, 131, 243–
627 263.
628 Lam, F., Gehloff, M., and Closen, M. (2010). "Moment-resisting bolted timber connections."
629 *Proceedings of the Institution of Civil Engineers: Structures and Buildings*, 163(4), 267–274.
630 Lam, F., Schulte-Wrede, M., Yao, C. C., and Gu, J. J. (2008). "Moment resistance of bolted timber
631 connections with perpendicular to grain reinforcements." *10th World Conference on Timber*
632 *Engineering 2008*, 2, 978–985.
633 Lau, P. H. (2006). "Fire resistance of connections in laminated veneer lumber (LVL)." Master
634 thesis, University of Canterbury,
635 Leijten, A. J. and Brandon, D. (2013). "Advances in moment transfering dvw reinforced timber con-
636 nections – Analysis and experimental verification, Part 1." *Construction and Building Materials*,
637 43, 614–622.
638 Leijten, A. J. M. (1998). "Densified Veneer Wood Reinforced Timber Joints with Expanded Tube
639 Fasteners. The Development of a New Joint." Phd thesis, Delft University, The Netherlands,
640 Lemaître, R., Epinal, F., Bocquet, J.-F., Schweigler, M., and Bader, T. K. (2018). "Beam-on-
641 foundation modelling as an alternative design method for single fastener connections." *Design*
642 *of Connections in Timber Structures*, 207.
643 Li, Z., He, M., and Wang, K. (2018). "Hysteretic Performance of Self-Centering Glulam Beam-to-

644 Column Connections." *Journal of Structural Engineering (United States)*, 144(5), 1–12.
645 Madhoushi, M. and Ansell, M. P. (2003). "Fatigue and cyclic loading of moment-resisting structures
646 connected using glued-in GFRP rods." p. 347 – 352.
647 Mischler, A. (2001). "Multiple Shear Steel-to-Timber Connections with Self-Drilling Dowels."
648 *Report no.*
649 New Zealand Standards (1993). "NZS3603:1993 Timber structures standard.
650 New Zealand Standards (1997). *NZS 3404: Part 1:1997 - Steel Structure Standard*. New Zealand
651 Standards, Wellington, New Zealand.
652 Newcombe, M. P., Pampanin, S., and Buchanan, A. H. (2010). "Global response of a two storey
653 Pres-Lam timber building." *New Zealand Society for Earthquake Engineering Conference*, 8(28),
654 8.
655 Nokes, R. (2017). *Streams: System Theory and Design*. Christchurch, New Zealand.
656 Ottenhaus, L. M., Li, M., Nokes, R., Cammock, P., and McInnes, B. (2019). "Use of particle
657 tracking velocimetry in timber material and connection testing." *European Journal of Wood and*
658 *Wood Products*, 77(2), 195–209.
659 Palermo, A., Pampanin, S., Buchanan, A. H., and Newcombe, M. P. (2005). "Seismic design of
660 multi-storey buildings using laminated veneer lumber (LVL)." *New Zealand Society for Earth-*
661 *quake Engineering Conference*, (14), 8.
662 Pino, D. M., Pampanin, S., Carradine, D., Deam, B., and Buchanan, A. H. (2010). "Dynamic
663 response of a multi-storey post-tensioned timber building." *11th World Conference on Timber*
664 *Engineering 2010, WCTE 2010*, 4, 2958–2965.
665 Porteous, J. and Kermani, A. (2013). *Structural timber design to Eurocode 5*. John Wiley & Sons.
666 Rodd, P. D. (1996). "Resin injected dowels in moment transmitting joints." *Proceedings of Inter-*
667 *national Wood Engineering Conference, New Orleans, USA*.
668 Rodd, P. D. and Leijten, A. J. M. (2003). "High-performance dowel-type joints for timber struc-
669 tures." *Progress in Structural Engineering and Materials*, 5(2), 77–89.
670 Rothoblaas (2017). "WS Self-perforating dowel." *Report no.*, Rothoblaas,

671 <https://www.rothoblaas.com/products/fastening/screws/screws-structures/ws#documents>.
672 Rothoblaas (2019). *SBD self-drilling dowel*, <https://www.rothoblaas.com/products/fastening/brackets-
673 and-plates/pins-bolts-metric/sbd#documents>.
674 Sawata, K., Sasaki, T., and Kanetaka, S. (2006). "Estimation of shear strength of dowel-type timber
675 connections with multiple slotted-in steel plates by European yield theory." *Journal of Wood
676 Science*, 52(6), 496–502.
677 Schober, K. U., Harte, A. M., Kliger, R., Jockwer, R., Xu, Q., and Chen, J. F. (2015). "FRP
678 reinforcement of timber structures." *Construction and Building Materials*, 97, 106–118.
679 Schreyer, A. C., Lam, F., and Prion, H. G. L. (2004). "Comparison of Slender Dowel-Type Fasteners
680 for Slotted-in Steel Plate Connections under Monotonic and Cyclic Loading." *World Conference
681 on Timber Engineering 2004*, 1–6.
682 Shu, Z., Li, Z., Yu, X., Zhang, J., and He, M. (2019). "Rotational performance of glulam bolted
683 joints: Experimental investigation and analytical approach." *Construction and Building Materi-
684 als*, 213, 675–695.
685 Smith, T., Ponzo, F. C., Di Cesare, A., Pampanin, S., Carradine, D., Buchanan, A. H., and Nigro,
686 D. (2014). "Post-tensioned glulam beam-column joints with advanced damping systems: Testing
687 and numerical analysis." *Journal of Earthquake Engineering*, 18(1), 147–167.
688 Sun, X., He, M., and Li, Z. (2020). "Novel engineered wood and bamboo composites for structural
689 applications: State-of-art of manufacturing technology and mechanical performance evaluation."
690 *Construction and Building Materials*, 249(1239), 118751.
691 Tlustochowicz, G., Serrano, E., and Steiger, R. (2011). "State-of-the-art review on timber con-
692 nections with glued-in steel rods." *Materials and Structures/Materiaux et Constructions*, 44(5),
693 997–1020.
694 van Bakel, R., Rinaldin, G., Leijten, A. J., and Fragiacomo, M. (2017). "Experimental–numerical
695 investigation on the seismic behaviour of moment-resisting timber frames with densified ve-
696 neer wood-reinforced timber joints and expanded tube fasteners." *Earthquake Engineering and
697 Structural Dynamics*, 46(8), 1307–1324.

698 Vašek, M. (2008). "Semi rigid timber frame and space structure connections by glued-in rods."
699 *World Conference on Timber Engineering 2008 Conference Proceedings*, number S 207.
700 Wang, C.-l., Lyu, J., Zhao, J., and Yang, H. (2020). "Experimental investigation of the shear char-
701 acteristics of steel-to-timber composite joints with inclined self-tapping screws." *Engineering*
702 *Structures*, 215(April), 110683.
703 Wang, M., Song, X., Gu, X., and Tang, J. (2019). "Bolted glulam beam-column connections under
704 different combinations of shear and bending." *Engineering Structures*, 181(July 2018), 281–292.
705 Wang, M., Song, X., Gu, X., Zhang, Y., and Luo, L. (2015). "Rotational behavior of bolted beam-
706 to-column connections with locally cross-laminated glulam." *Journal of Structural Engineering*
707 *(United States)*, 141(4), 1–7.
708 Wanninger, F. and Frangi, A. (2016). "Experimental and analytical analysis of a post-tensioned
709 timber frame under horizontal loads." *Engineering Structures*, 113, 16–25.
710 Yang, H., Liu, W., and Ren, X. (2016). "A component method for moment-resistant glulam beam-
711 column connections with glued-in steel rods." *Engineering Structures*, 115, 42–54.
712 Zarnani, P. and Quenneville, P. (2013). *Timber Rivet connections design guide*,
713 <http://assets1.expan.co.nz/assets/EXPAN-Design-Example—Timber-rivet-base-connection-
714 June-2013.pdf>.
715 Zhang, C. (2018). "Reinforcement of Timber Dowel-Type Connections Using Self-Tapping Screws."
716 Phd thesis, University of Bath,
717 Zhang, C., Guo, H., Jung, K., Harris, R., and Chang, W. S. (2019). "Using self-tapping screw to
718 reinforce dowel-type connection in a timber portal frame." *Engineering Structures*, 178(October
719 2018), 656–664.

List of Tables

TABLE 1. Test matrix

Group	Description	No. of replicates
USM	Unreinforced specimen under monotonic loading	1
USC	Unreinforced specimen under cyclic loading	3
RSC	STS-reinforced specimen under cyclic loading	3

TABLE 2. The spacing information of specimens and Eurocode 5 (unit: mm)

Spacing	Dowel spacing in JPB	Eurocode 5 specification
a_1 (parallel to grain)	50 (6.7d)	37.5(5d)
a_2 (perpendicular to grain)	88 (11.7d)	22.5 (3d)
a_{3t} (loaded end)	80 (10.7d)	max(80, 7d)
a_{4t} (loaded edge)	50 (6.7d)	30 (4d)

Note: d is the diameter of fastener.

TABLE 3. Material properties

Members	Materials	Properties (characteristic values)
Beams and columns	GL10 New Zealand Radiata Pine (1993)	Bending strength $f_b = 22\,\text{MPa}$ Compression strength parallel to grain $f_c = 26\,\text{MPa}$ Tension strength parallel to grain $f_t = 11\,\text{MPa}$ Compression strength perpendicular to grain $f_{cp,0} = 8.9\,\text{MPa}$ Shear strength $f_s = 3.7\,\text{MPa}$ Modulus of elasticity $E_{GL} = 10\,\text{GPa}$ Modulus of rigidity $G_{GL} = 670\,\text{MPa}$
Inserted steel plates	6 mm thick Grade 300 flat plate (1997)	Nominal yield strength $f_y = 300\,\text{MPa}$ Modulus of elasticity $E_S = 200\,\text{GPa}$
SDD	Rothoblaas SBD type $\phi 7.5 \times 235$ (2019)	Yield moment $M_{y,Rk} = 81\,266\,\text{N} \cdot \text{mm}$
STS for reinforcement	SPAX fully-threaded cylinder head STS $\phi 8 \times 450$ (2017)	Tensile strength $f_{tens,k} = 17\,\text{kN}$ Withdrawal parameter $f_{ax,k} = 12\,\text{N/mm}^2$

TABLE 4. A summary of connection performance parameters

Parameters	USM-1	USC-1	USC-2	USC-3	USC-Avg	RSC-1	RSC-2	RSC-3	RSC-Avg	Increase in Avg (%)
Δ_y (°)	0.8	0.9	0.9	0.7	*0.8*	0.8	0.9	0.8	*0.8*	0
M_y (kN· m)	122.5	116.5	129.0	116.0	*120.5*	127.4	133.0	127.0	*129.1*	7
K_y (kN· m/°)	154.2	143.5	156.6	165.4	*155.2*	156.6	153.3	162.2	*157.4*	1
Δ_{peak} (°)	1.6	1.4	1.5	0.8	*1.2*	1.8	1.8	1.7	*1.8*	50
M_{peak} (kN· m)	138.1	128.6	145.0	118.6	*130.7*	149.6	153.0	145.5	*149.4*	14
Δ_u (°)	1.6	1.6	1.8	0.8	*1.4*	3.3	3.3	4.5	*3.7*	164
M_u (kN· m)	110.5	102.9	121.1	99.1	*107.7*	119.6	122.4	116.4	*119.5*	11
μ	2.0	1.8	2.0	1.2	*1.7*	4.1	3.7	5.6	*4.5*	164

Note: 1. Avg =average value.
2. Increase in Avg is the increase percentage of RSC-Avg when compared to the USC-Avg.

TABLE 5. Comparison of the test results with connection tests in literature

Tests	Beam cross section ($mm \times mm$)	Fasteners	M_y (kN · m)	Δ_y (°)	M_{peak} (kN · m)	Δ_{peak} (°)
Group USC	450×315	$16 \times \phi 7.5$ SDD	120.5	0.8	130.7	1.2
Group RSC	450×315	$16 \times \phi 7.5$ SDD	129.1	0.8	149.4	1.8
Lam et al. (2008)	304×130	$4 \times \phi 19.1$ cap screws	41.8	3.0	62.5	15.9
Lam et al. (2010)	304×130	$4 \times \phi 25.4$ bolts	**84.8**	2.4	**105.9**	6.8
Leijten and Brandon (2013)	300×150	$4 \times \phi 18$ expanded tubes	n/a	n/a	40.0	6.7
He and Liu (2015)	300×200	$4 \times \phi 24$ bolts	27.1	6.4	32.0*	12.2*
He et al. (2016)	384×150	$4 \times \phi 16$ bolts	28.0	1.5	68.5	10.5
He et al. (2017)	260×130	$6 \times \phi 16$ bolts	19.8	1.2	22.0	2.2
Karagiannis et al. (2017)	280×140	$20 \times \phi 10$ bolts	51.4	1.3	54.4	7.4
van Bakel et al. (2017)	600×116	$4 \times \phi 35$ expanded tubes	**107.9**	0.2	**128.0***	1.3*
Zhang (2018)	300×140	$9 \times \phi 12$ dowels	n/a	n/a	13.9	5.0*
Wang et al. (2019)	305×130	$4 \times \phi 20$ bolts	10.0	4.3	20.0	9.5
Shu et al. (2019)	320×180	$4 \times \phi 24$ bolts	n/a	n/a	26	4.9*

Note: 1. The moment capacity and rotation are the mean values of the strongest group reported in each paper.
2. Numbers with a "*" symbol are estimated from load-slip curves in the publications.

TABLE 6. Connection strength predictions

Tests or model	M_y (kN · m)	M_{peak} (kN · m)
Group RSC	129.1	149.4
Porteous and Kermani (2013)	76.6*	n/a
Zhang (2018)	n/a	88.5
Shu et al. (2019)	n/a	109.6

Note: 1. The moment is calculated by $M = F_V H$ for all analytical models.
2. The value with "*" is defined as the characteristic moment capacity in the paper.

TABLE 7. Stiffness predictions

Stiffness	k_u (kN/mm)	$K_{B,y}$ (kN · m/°)	$K_{B,peak}$ (kN · m/°)	$K_{C,y}$ (kN · m/°)
Eurocode 5	17.5	189.4	44.0	450.4
Test-based	12.9	140.0	32.5	332.9

TABLE 8. Analytical predictions of rotation

State	$M_{B,O'}$ (kN · m)	$M_{C,O''}$ (kN · m)	Δ_B (°)	Δ_C (°)	Δ_{an} (°)	Δ_{exp} (°)
Yield moment state	65.7	80.9	0.4 (0.5)	0.1 (0.2)	0.5 (0.7)	0.8
Peak moment state	91.7	105.6	1.0 (1.3)	0.2 (0.3)	1.2 (1.6)	1.8
Ultimate moment state	73.4	84.5	3.1	0.2 (0.3)	3.3 (3.4)	3.7

Note: The rotation values in parentheses are based on $k_{u,2}$.

List of Figures

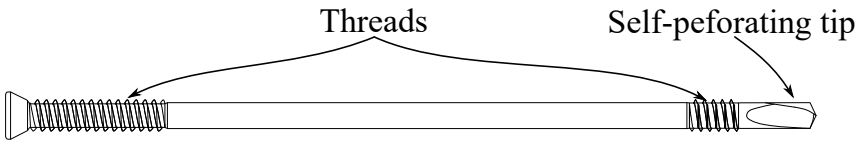

Fig. 1. Self-drilling dowel product (Rothoblaas 2019)

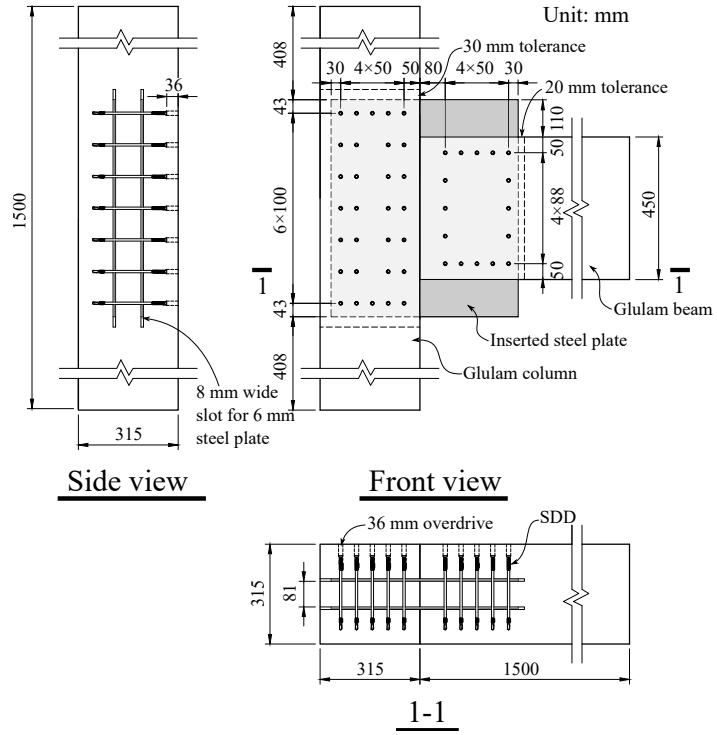

(a) Specimen without STS reinforcement (USM and USC)

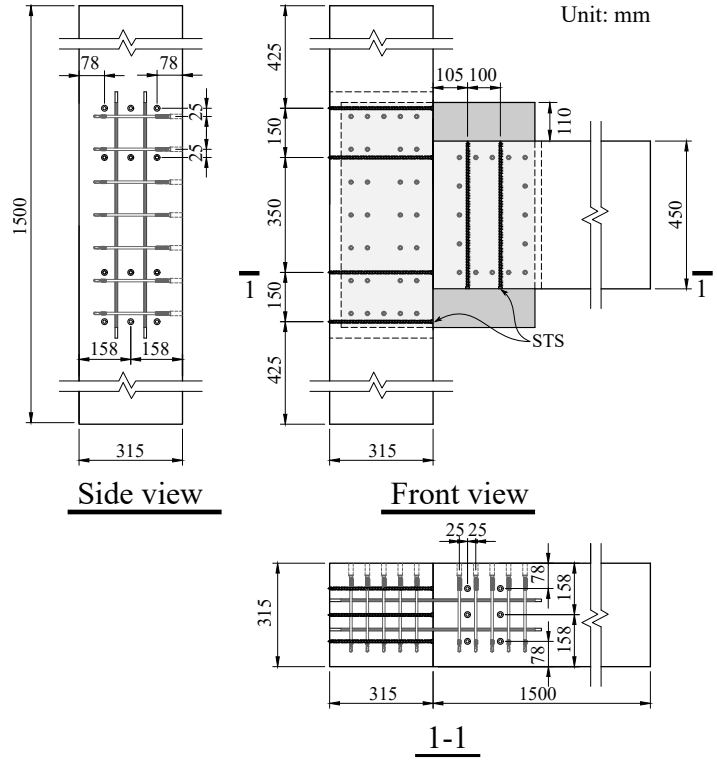

(b) Specimen with STS reinforcement (RSC)

Fig. 2. Specimen design details

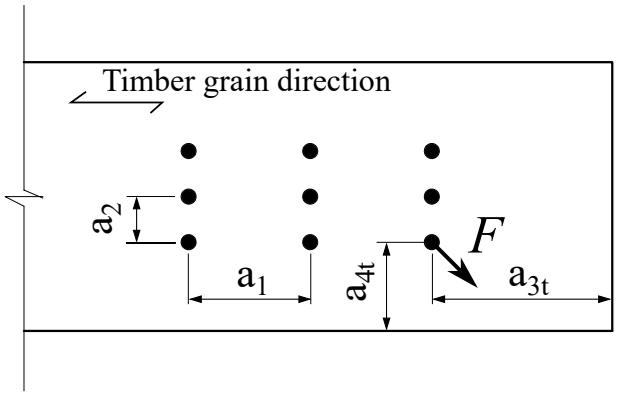

Fig. 3. Spacing and end and edge distance notations in Eurocode 5

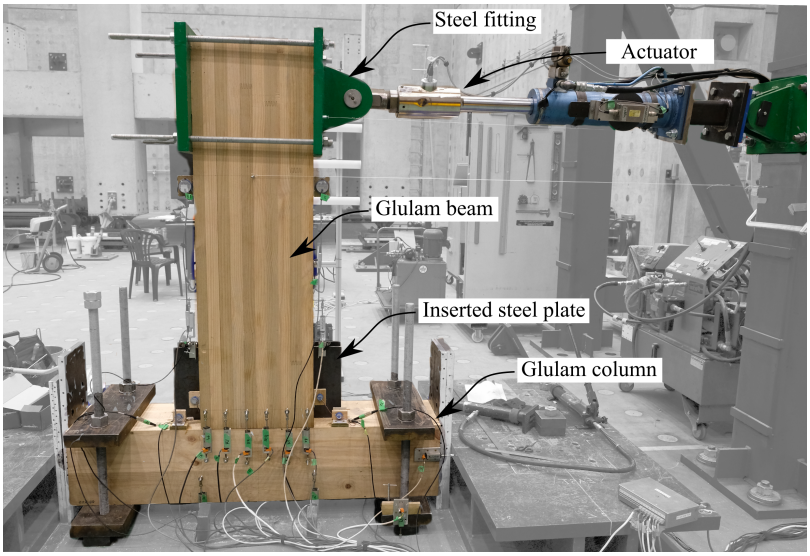

(a) Test setup

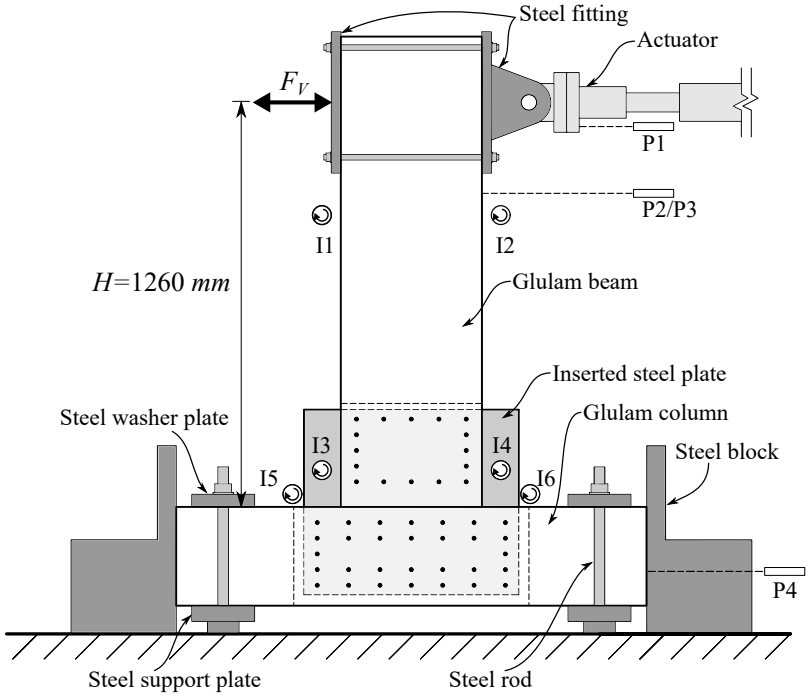

(b) Instrumentation

Fig. 4. Test setup and instrumentation

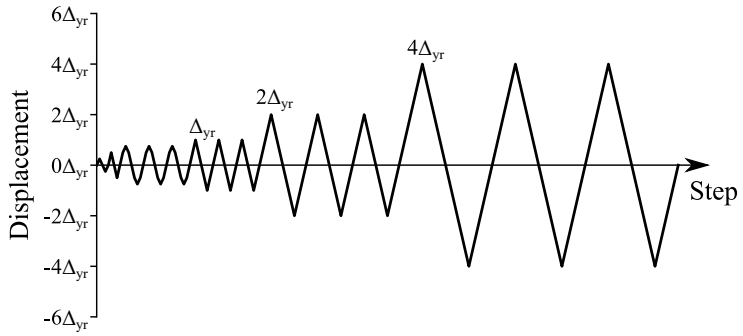

Fig. 5. Cyclic loading protocol according to EN 12512

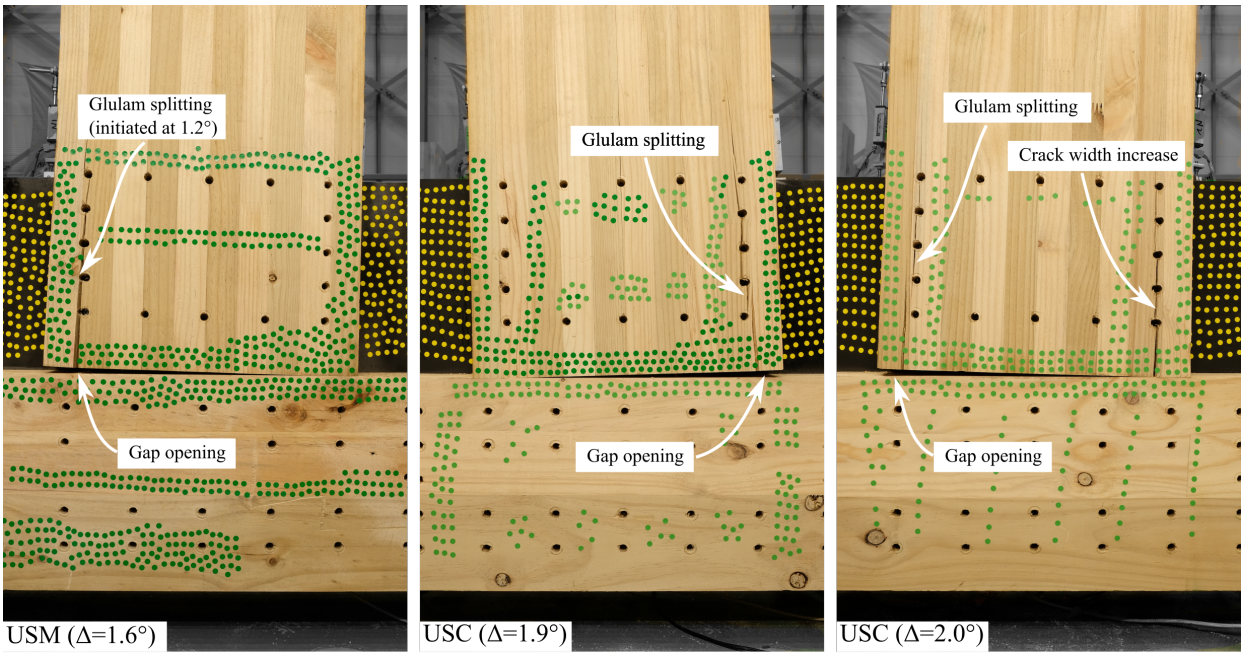

Fig. 6. Failure modes in unreinforced specimens (USM and USC)

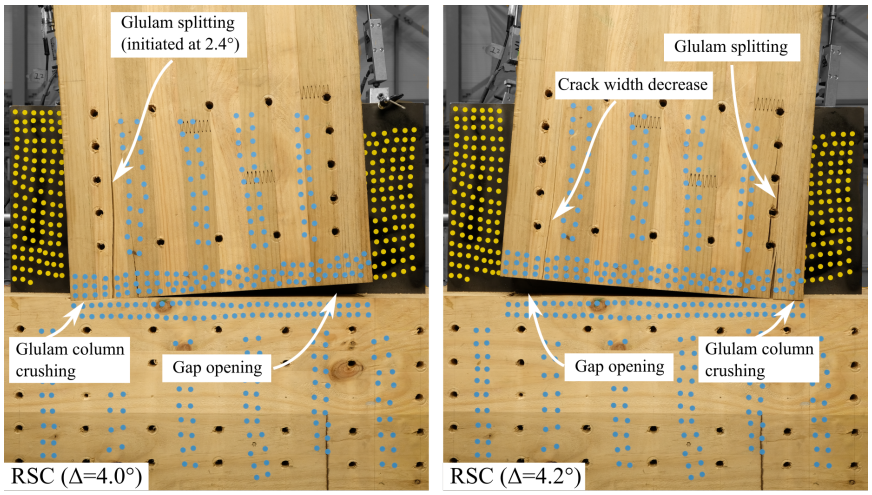

Fig. 7. Failure modes in reinforced specimens (RSC)

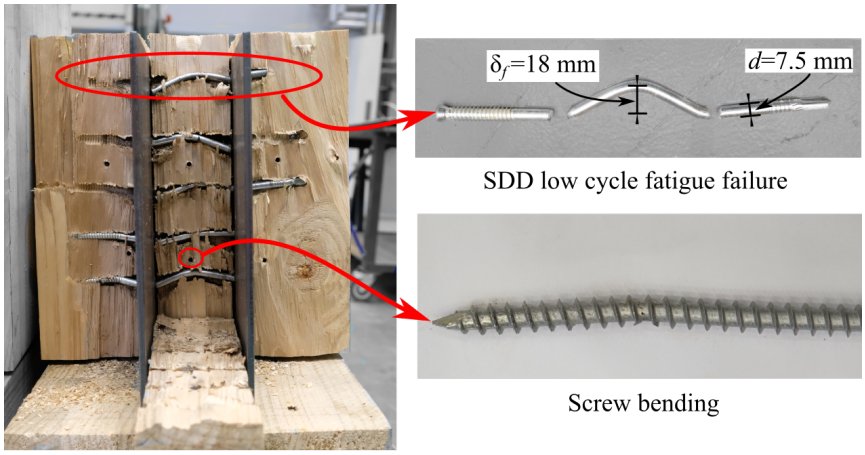

Fig. 8. Failure modes of SDD in RSC specimens

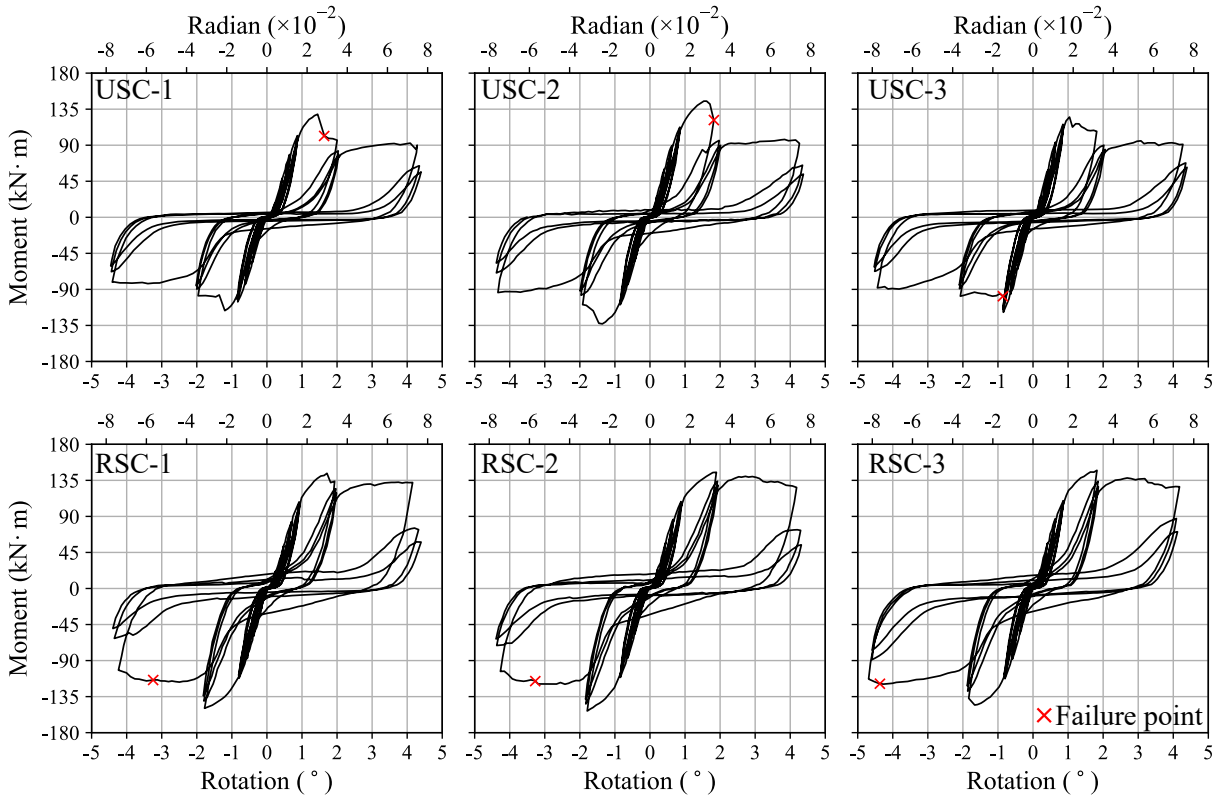

Fig. 9. Moment-rotation hysteresis curves

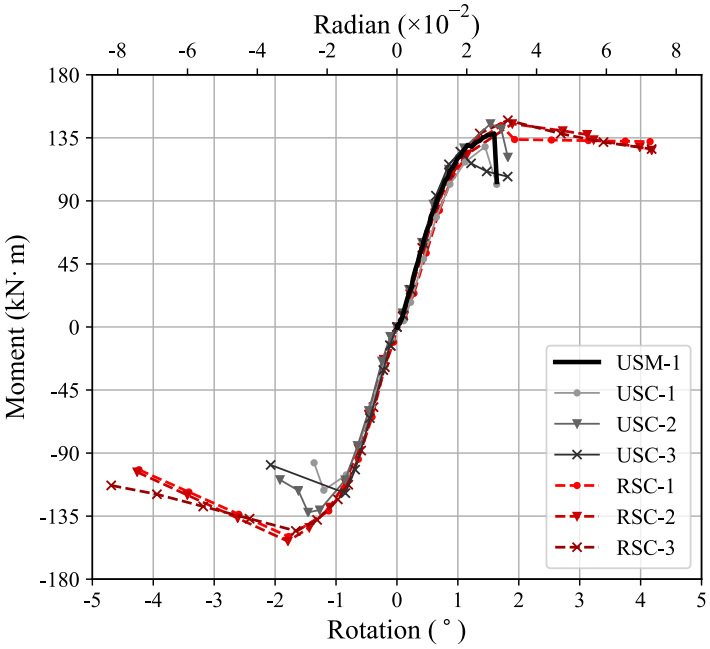

Fig. 10. Backbone curves of specimens

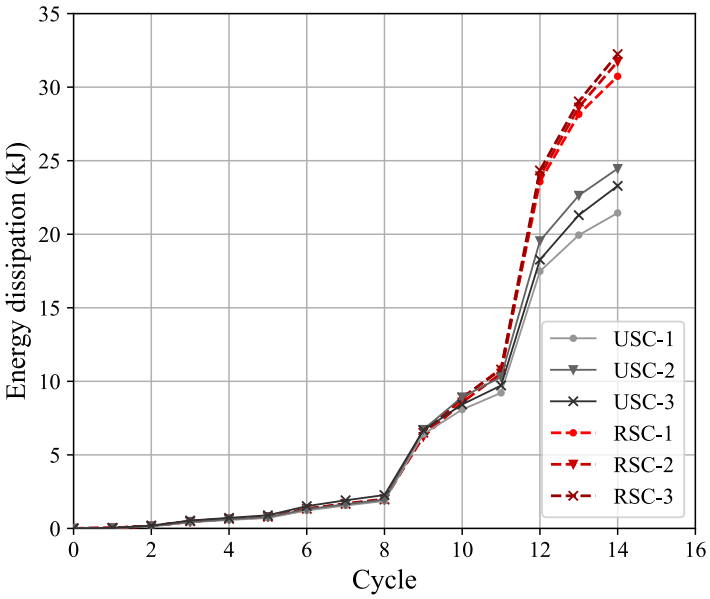

Fig. 11. Energy dissipation of specimens

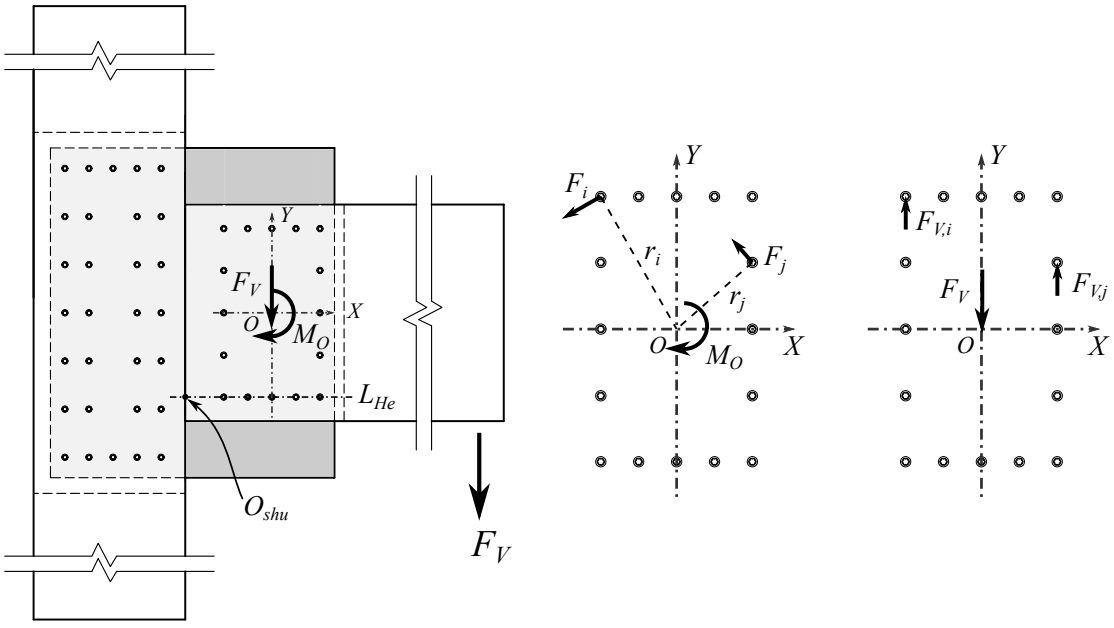

(a) (b) (c)

Fig. 12. Analytical models in literature

(a) CR assumptions in literature; (b) Moment distribution assumption by Porteous and Kermani (2013); and (c) shear force distribution assumption by Porteous and Kermani (2013)

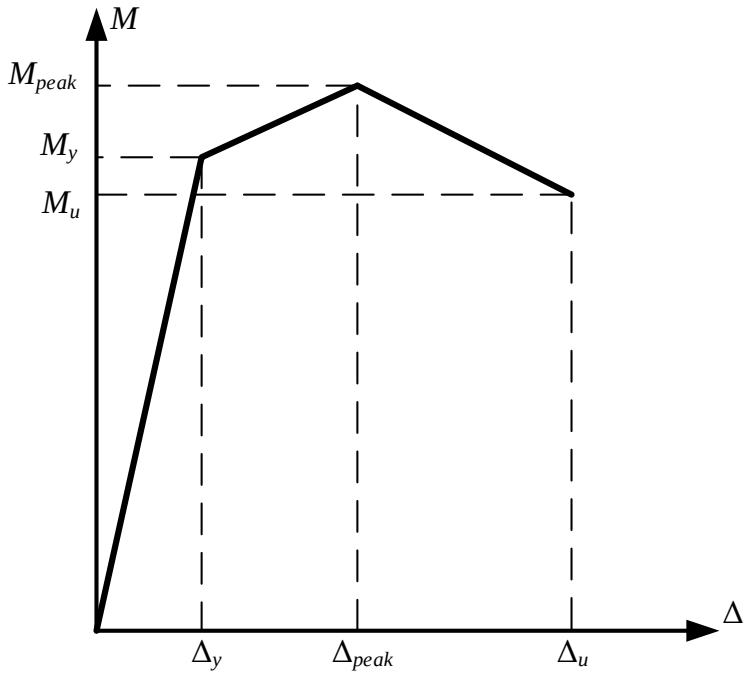

Fig. 13. Simplified moment-rotation relationship

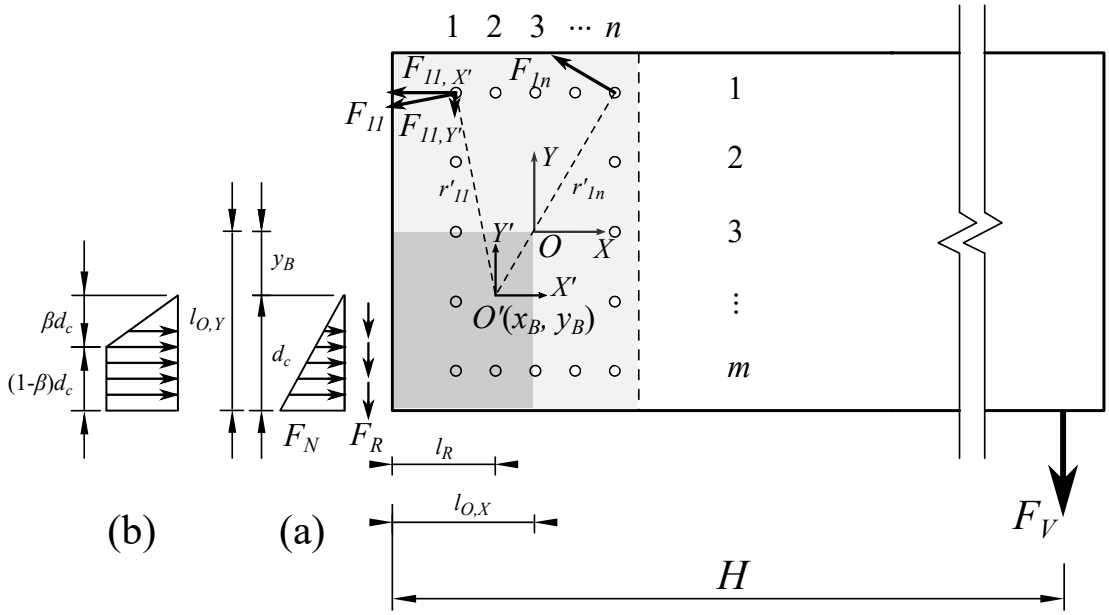

Note: (a) Stress distribution at the yield strength

(b) Stress distribution at the ultimate strength

Fig. 14. Load action of the beam

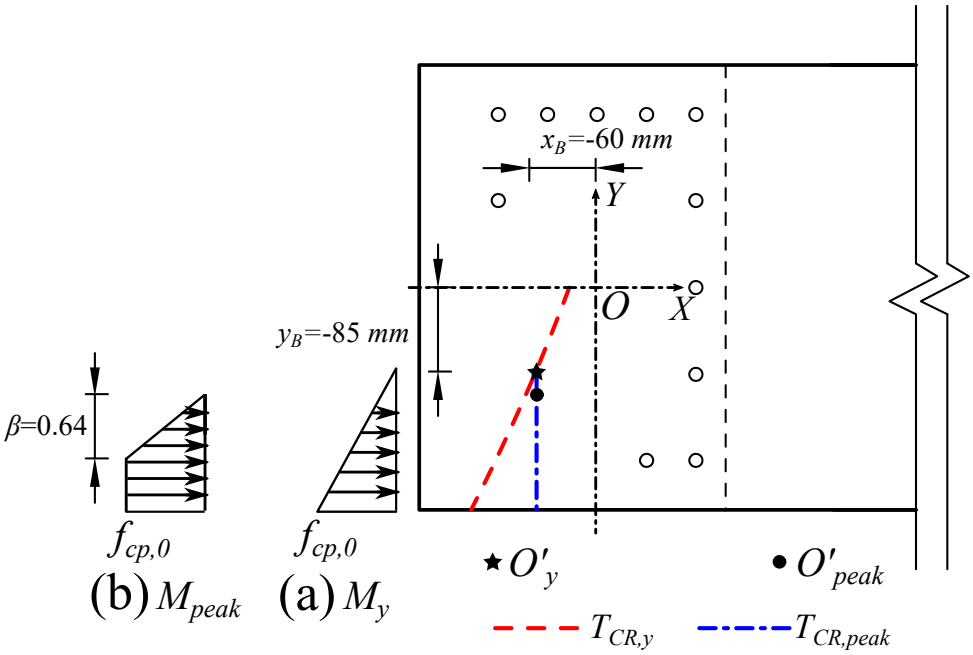

Fig. 15. The trajectory of CR

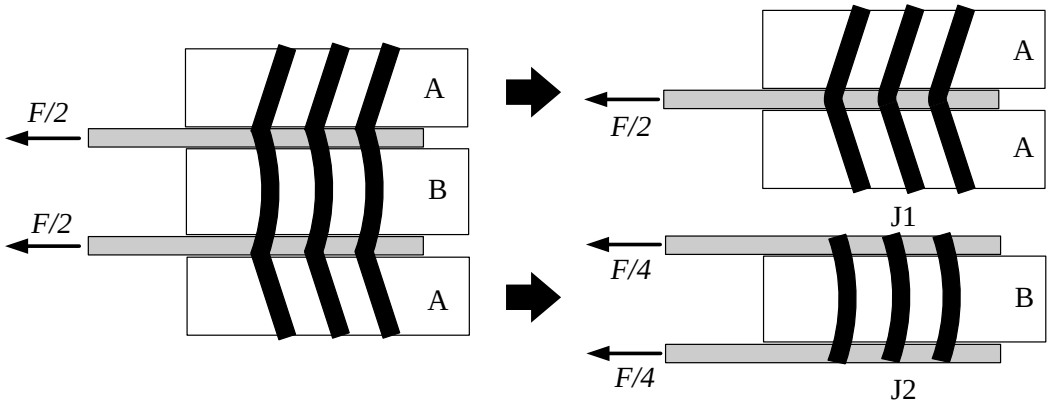

Fig. 16. Dowelled connection calculation model

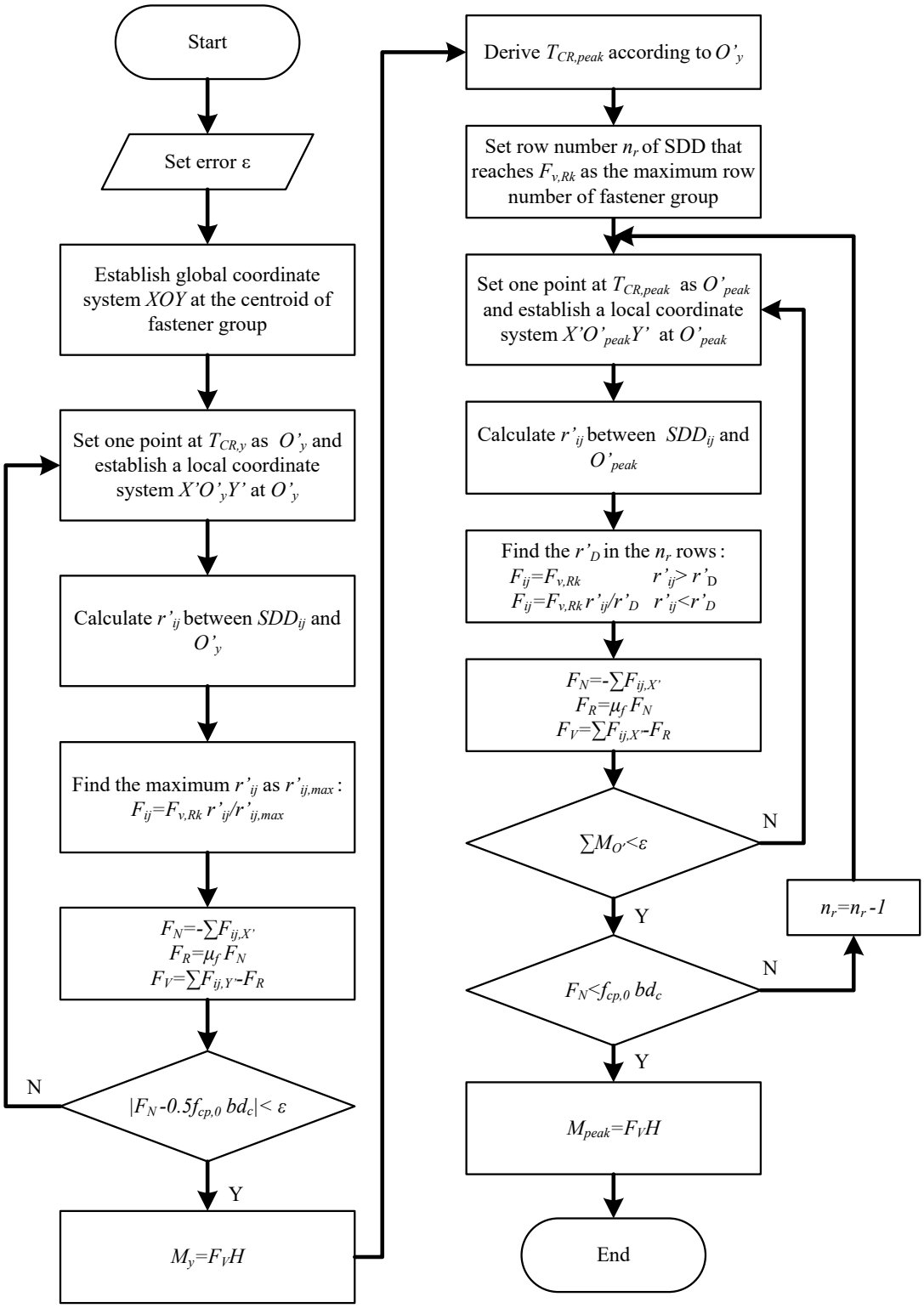

Fig. 17. Flowchart for calculating M_y and M_{peak}

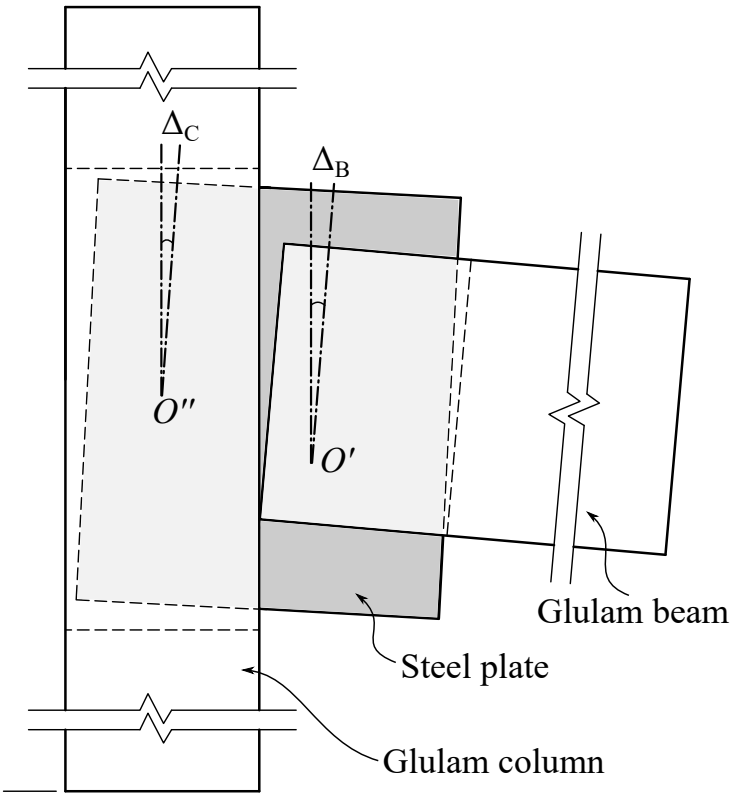

Fig. 18. Rotation components of the connection

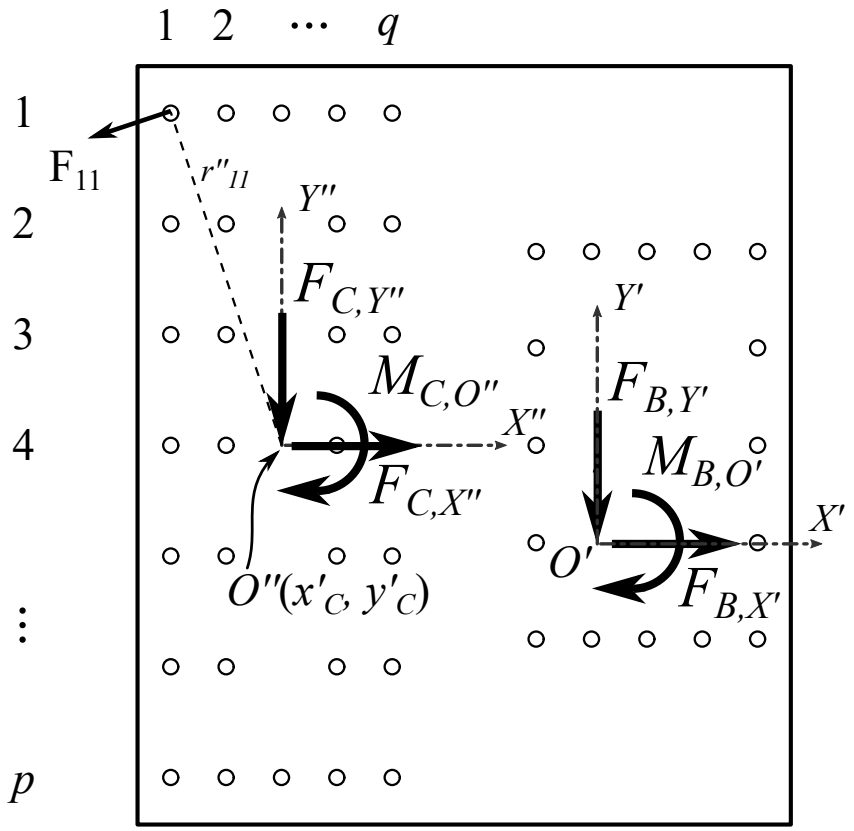

Fig. 19. Load action of the steel plate

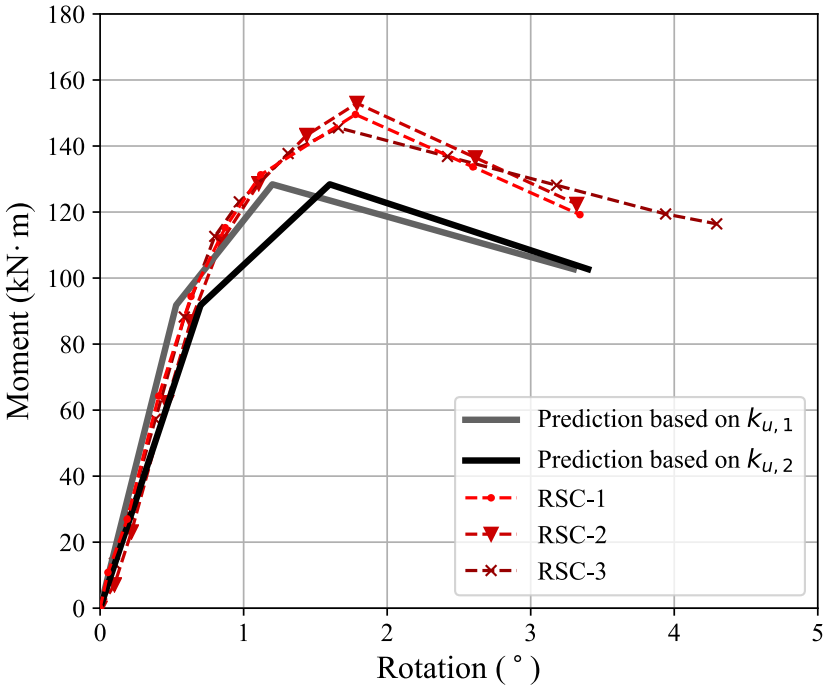

Fig. 20. Comparison of backbone curves

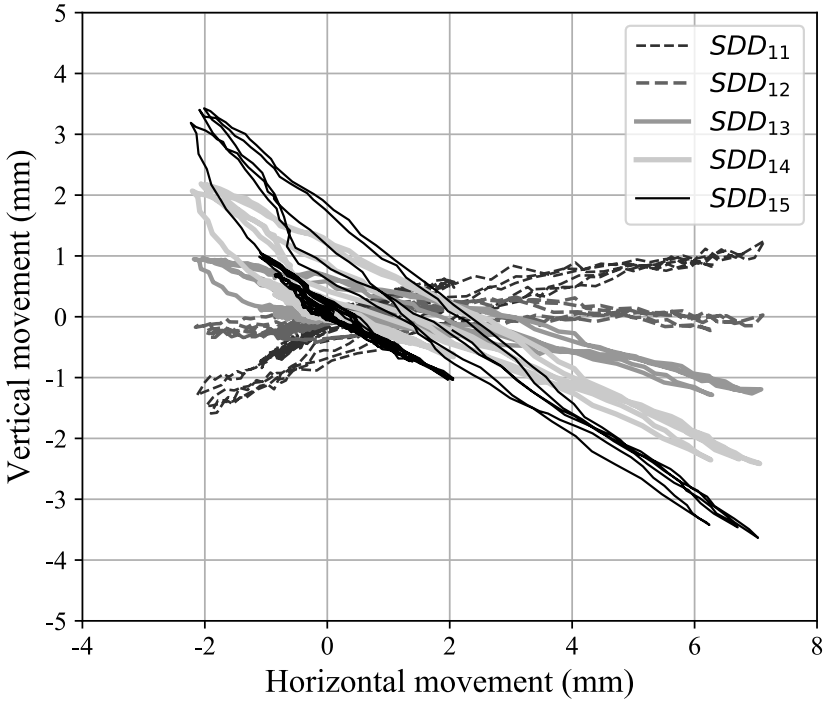

Fig. 21. SDD movement trajectory of RSC-1 by PTT

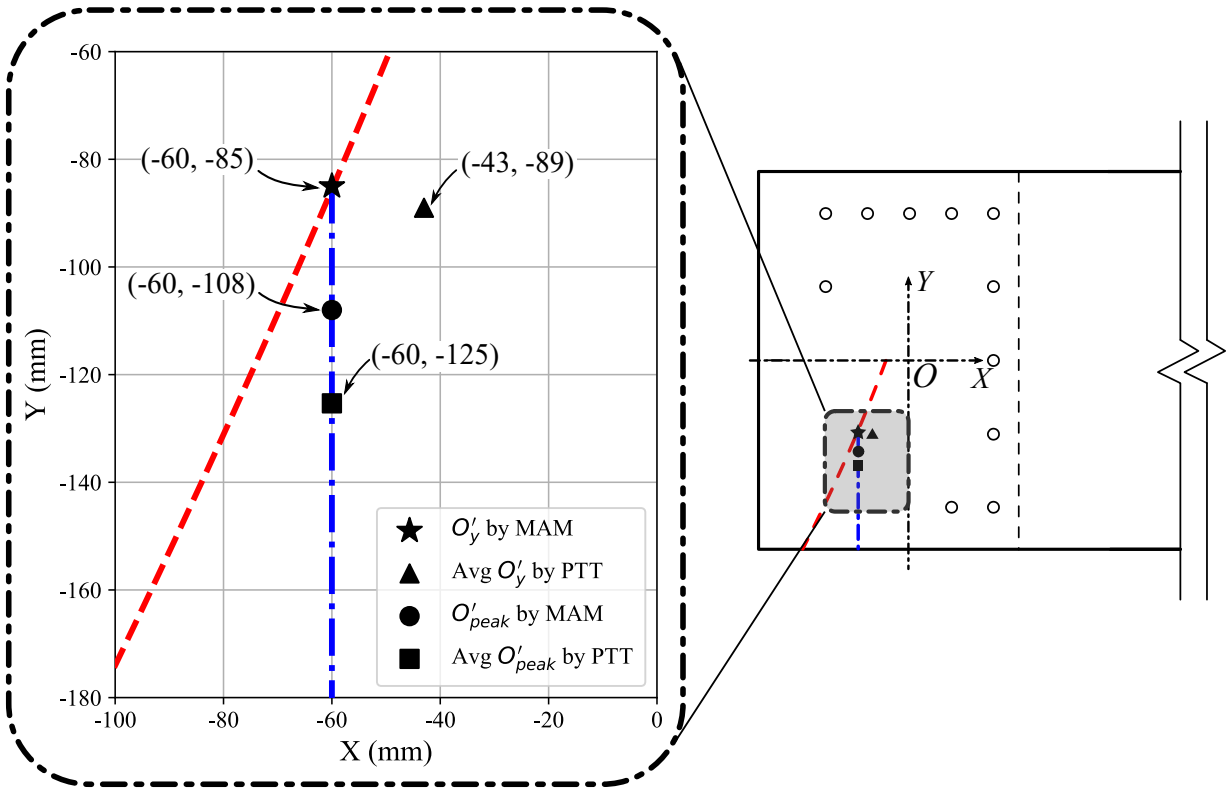

Fig. 22. Verification of CR at M_y and M_{peak}

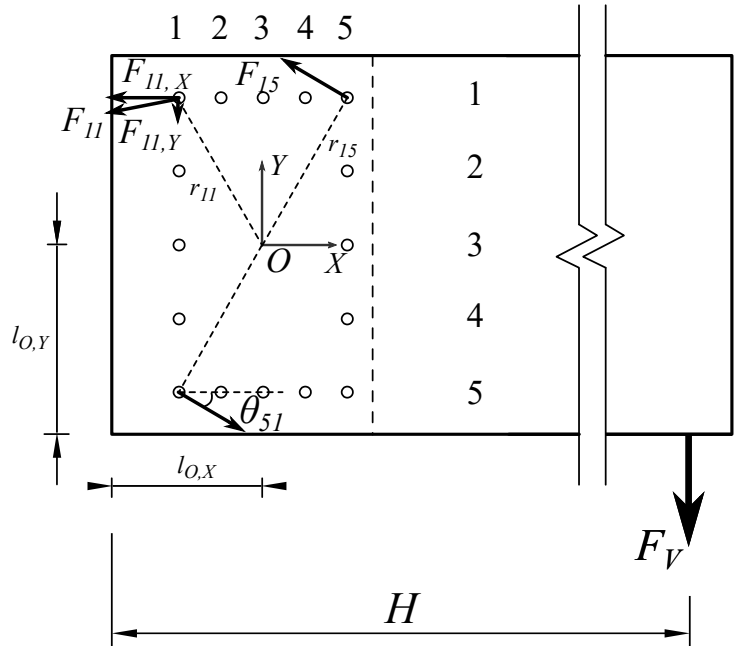

Fig. 23. Analytical model from Porteous and Kermani (2013)

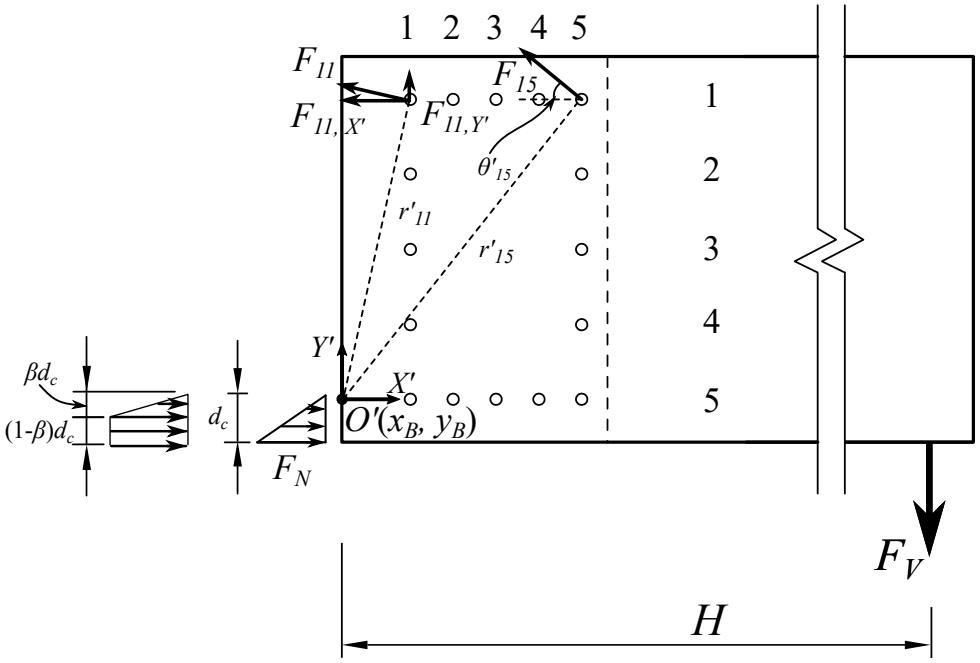

Fig. 24. Analytical model from Shu et al. (2019)